Superconducting Wiggler for Adone: Design and Present Status.

M. BARONE, A. CATTONI, U. GAMBARDELLA, G. MODESTINO
R. PARODI(*), R. PENCO(*), M. PERRELLA(*), M. PREGER
C. SANELLI, A. SAVOIA and F. SGAMMA

INFN, Laboratori Nazionali di Frascati - P.O. Box 13, 00044 Frascati, Italia
ABB Ansaldo Componenti - Genova, Italia

Summary. — A superconducting wiggler has been designed and built at Laboratori Nazionali INFN in Frascati, Italy, in collaboration with Ansaldo Componenti-Genova, to be used as an insertion device in the Adone storage ring. It will be used as a light source on the 1.5 GeV, 100 mA electron beam of the accelerator, to produce about 10^{12} photons/s/mrad in 0.1% band width, in the short X-ray wavelength range. In order to minimize the electron beam orbit distortion and to obtain the best phase space distribution of the generated synchrotron radiation (a single bright spot), a superconducting dipole, producing a sharp vertical field peak (6 T, 12 cm FWHM), between two normal conducting side dipoles (0.8 T), to compensate the field integral, has been manufactured. The s.c. dipole is made up of 2 NbTi coils, separated by a central plate and kept together by two 356 kg total weight iron yokes. The magnet gap is 6 cm and the design current is 360 A. The system is contained in a warm bore cryostat and cooled by boiling helium at 4.6 K. The static cryostat helium consumption is of 4 l/h and, when the cryomagnet is energized, it is cooled by a 1430S Koch liquefier/refrigerator on line with it through transfer lines. The stored energy is 184 kJ. This paper describes the latest status of the facility and the verification tests.

PACS 85.25 – Superconducting devices; superconducting magnets.

Introduction.

The aim of this facility is to shift the «universal» spectral curve of the synchrotron radiation from the Adone bending magnets towards higher-energy photons [1, 2]. At the energy of 1.5 GeV ($B_{\text{bending}} = 1$ T) and for a circulating beam of 100 mA, the emitted photons/s/mrad in 0.1% band width, at 1.5 keV critical energy, are about $2.4 \cdot 10^{12}$ (see fig. 1). The same flux can be obtained with photons of ≈ 9 keV critical
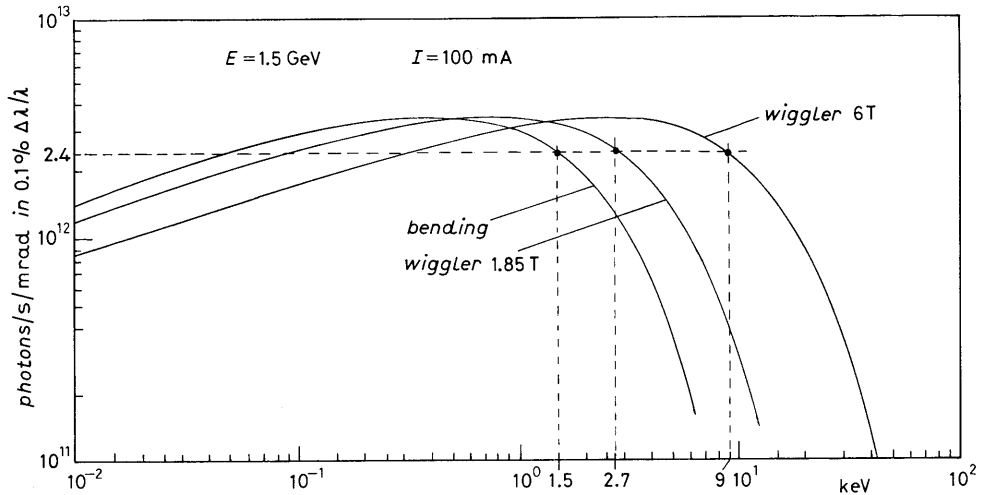
Fig. 1. – Wavelength spectrum of synchrotron radiation for the maximum field in the superconducting wiggler (6T).

energy by generating on the beam trajectory a 6 T magnetic field. It is well known, from the fundamental laws of synchrotron light emission, that the photon critical energy is given by

$$(1) \qquad \varepsilon_c = 12.4/\lambda_c = (2/3)BE^2$$

with ε_c in keV, λ in Å, B in T and E in GeV, and furthermore that

$$(2) \qquad P/I = 3.312 \cdot 10^{-6}\gamma^2 \int B^2 \, ds$$

with P/I in W/A and s in cm, which means that, in addition, the radiated power will increase with B^2.

The problem is to insert in a straight section of the storage ring a special magnet, called wiggler, without causing destructive perturbations to the beam itself.

Another important aspect is the structure of the synchrotron light source to be obtained, namely its horizontal and vertical phase space distribution. The source created by a wiggler has in general a structure in both planes, whose complexity depends on the number of «wiggles» (electron orbit oscillations in the wiggler). On the other hand, to be compatible with the storage ring optics, the wiggler must fulfill the following conditions:

1) $\int B_z \, ds \approx 0$ (the first integral of the field vertical components should vanish).

2) The orbit parameters, displacement and angle, at the entrance of the wiggler should be the same at the exit. (This implies the symmetry of the field distribution along the beam trajectory, with a symmetry axis orthogonal to the straight section, lying on the orbit plane and passing through the wiggler centre).

To reach the goal of having a very simple light source structure and a

compensated magnetic field integral, a peculiar magnetic field pattern along the beam trajectory has been adopted: a sharp vertical field peak ($-6\,T$, 12 cm FWHM) at the straight section centre, compensated by two side tails (both decreasing from $+0.8\,T$ to zero in more than 1 m of free straight section length).

The chosen field profile and symmetry drive the electrons on a single orbit bump in the horizontal plane, which is also the orbit plane of the unperturbed storage ring. A single «wiggle» creates a single bright spot in the horizontal (and vertical) phase space.

The magnetic structure is composed of a superconducting 6 T dipole, placed in a warm bore cryostat, and two (warm) side dipoles for the field compensation.

The project requires solving the following problems:

I   Tridimensional field mapping in order to evaluate the magnetic-field profile along the beam trajectory. Electron orbit in the wiggler.
II   Intensity and phase space distribution of the photon source.
III Effects of the superconducting wiggler on storage ring parameters.
IV   Electromagnetic design. Superconducting cable choice. Power supply and controls. Quench protection.
V   Cryogenic design. Cryostat and helium liquefier/refrigerator characteristics.
VI   Mechanical design. Finite element method structural analysis of the most critical parts.
VII Compensator magnet design.
VIII Magnetic measurement system design (for point-to-point and integral field measurement). Dedicated data acquisition system. Flip coils and Hall probe actuators design.
IX   Wiggler alignment and position control.

A brief description of these subjects and the adopted solutions, together with some bibliography to supply more details, is given in the following sections.

1. – Tridimensional field mapping in order to evaluate the magnetic-field profile along the beam trajectory. Electron orbit in the wiggler.

The magnetic field profile along the Adone straight section, produced by the superconducting dipole and by the two compensator magnets, is shown in fig. 2. The
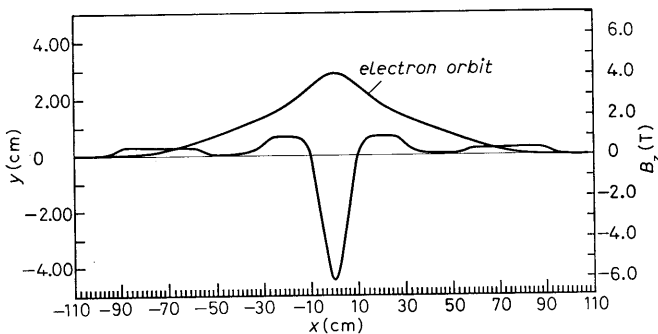

Fig. 2. – Beam orbit and magnetic-field profile along the Adone straight section, produced by the superconducting dipole and by the two compensator magnets (PROFI).

unperturbed electron orbit lies on the horizontal plane which is a symmetry plane and a field equipotential of the system. The field profile belongs to the only nonvanishing component of the magnetic field on that plane, the vertical one. This field profile has been obtained by studying the magnetic problem with computer programs allowing the analysis of the three magnets whose irons are not connected: Poisson (bidimensional), Profi (CERN) and Magnus (LNF). Profi and Magnus (ref. [3]) are tridimensional codes so that they allow the estimate of the side fringing and the evaluation of the magnetic-field terms integrated along the electron beam trajectory.

The electromagnetic calculation has also been checked, but only for the superconducting dipole, by «Ansaldo Componenti», the factory which has built the magnet, using the tridimensional code Tosca. Ansaldo has also verified the forces acting on the coils and on the iron, previously calculated by means of Poisson.

The tridimensional codes indicate the same magnetic field profile. One can compare fig. 2, where Profi calculation is reported, with fig. 3 obtained by Magnus, and fig. 4, predicted by Tosca. Differences of the order of 10^{-2} are found on the maximum field value at the gap centre (6.155 T Magnus, 6.08 T Tosca, 6.29 Profi). These differences are justified by small differences in coil current and are also due to the convergence tolerances of each code.
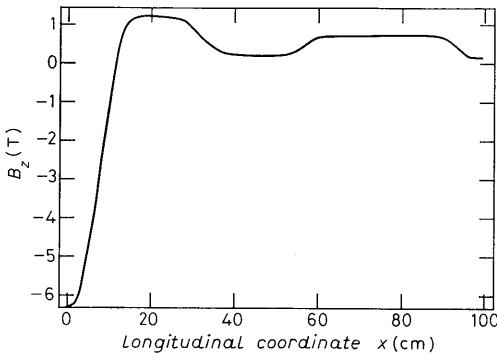

Fig. 3.   Fig. 4.

Fig. 3. – Vertical B component along the Adone straight section, produced by the superconducting dipole and by the two compensator magnets (MAGNUS).
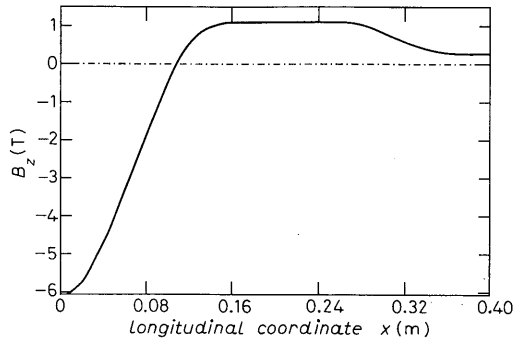
Fig. 4. – Vertical B component along the Adone straight section, produced by the superconducting dipole (TOSCA).

The tridimensional programs can also show the magnetic field profile along a direction orthogonal to the straight section (radial coordinate). The vertical component of the field along the radial coordinate, on the horizontal symmetry plane, is shown in fig. 5 as predicted by Magnus, and in fig. 6 as calculated with Tosca. The experimental data have been compared to the computed results. Figure 7 shows the field measurements, on the superconducting dipole, in good agreement with the output of Tosca and Magnus. Also the Profi predictions are, of course, well in agreement with the experimental points.

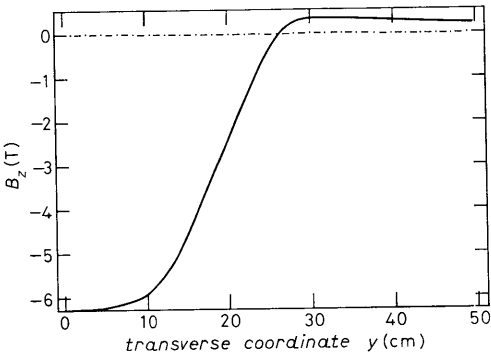The 1.5 GeV electron beam trajectory has been calculated making use of the

Fig. 5.

Fig. 6.

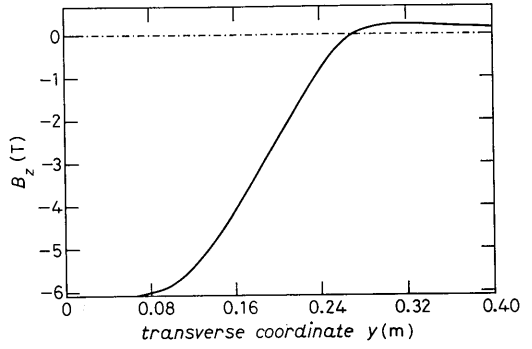Fig. 5. – Vertical B component along the radial axis on the symmetry plane (MAGNUS).

Fig. 6. – Vertical B component along the transverse axis on the symmetry plane (TOSCA).

results of different codes. The beam will have an orbit bump of ~ 3 cm, corresponding to the 6 T peak field. It would be desirable to have a radial field flat top of the same extent, so that the particles are not affected by multipolar field terms, the sextupole in particular, introduced by the wiggler. Since the iron saturates, this is not possible in spite of the remarkable radial width of the superconducting pole (± 12 cm). Nevertheless the field variation, corresponding to 3.5 cm beam displacement, is about $(0.25 \div 0.3)\%$ of the central field (see fig. 5 and fig. 6).
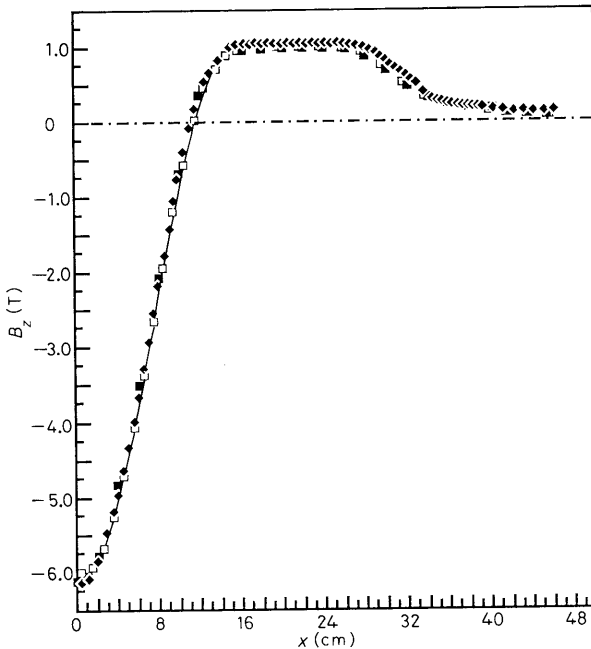

Fig. 7. – Computed and measured field. $\square$ B_z meas., $\blacklozenge$ B_z MAGNUS, $\blacksquare$ B_z TOSCA.

The sextupole term, integrated along the straight section, has been estimated; its value is not remarkable but, if necessary, it will be possible to cancel the sextupole introduced by the superconducting dipole by machining the pole profile of the compensator magnets.

2. – Intensity and phase space distribution of the photon source.

The spectrum and spatial distribution of the synchrotron radiation from the superconducting wiggler is rather different from the emission of a bending magnet, mainly because of the fast variation of the vertical magnetic field inside the central pole. If more than one beam line is to be installed on the wiggler straight section, each will have a peculiar photon energy spectrum and phase space distribution.

In order to give an approximate description of the photon source, the model described in ref. [4] has been adopted. The calculation is performed under the assumption of a perfectly flat beam, neglecting both the beam angular dispersion and the intrinsic aperture of the synchrotron radiation in the horizontal plane, which are much smaller than the typical angles of the electron trajectory in the wiggler. Each point of the beam path is taken into account as a source of radiation with the spectrum determined by the magnetic field at that point and the position and direction of the trajectory.

The energy spectrum corresponding to the maximum field ($\approx 6\,\mathrm{T}$) is shown in fig. 1, compared with the existing sources in the bending magnets and in the six-poles $1.85\,\mathrm{T}$ wiggler in Adone. For the sake of simplicity, the phase space plot of the source can be obtained by calculating the projection of each trajectory point onto the horizontal midplane of the wiggler. In this way each trajectory point can be represented as a cell in the source phase space, with an intensity proportional to the average number of photons in the desired wavelength range. Due to the longitudinal symmetry of the magnetic field with respect to the wiggler centre, the intensity distribution is symmetric with respect to the x-axis.
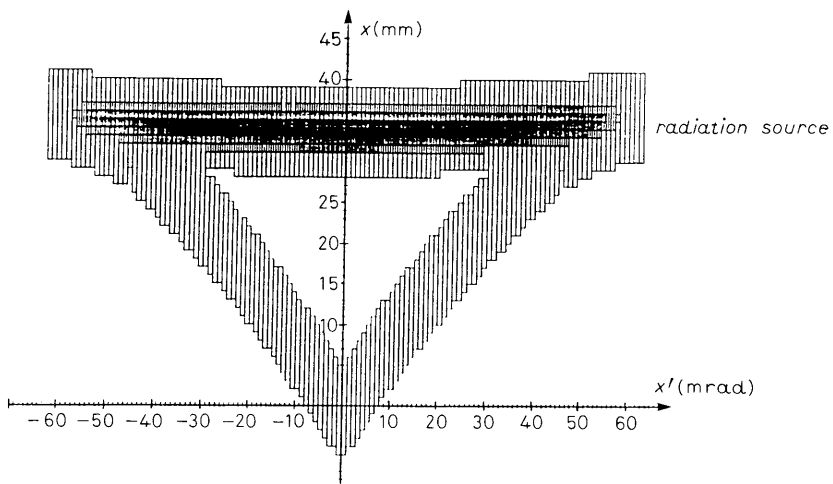

Fig. 8. – Phase space plot of the radiation from the superconducting wiggler: darker areas correspond to higher intensity.

Figure 8 shows an example of this phase plot for $\lambda = 1 \, \text{Å}$: the darker zones correspond to higher intensity. As can be seen from the plot, most of the radiation comes from a point displaced horizontally by $\approx 35 \, \text{mm}$ from the straight section axis, with an angular spread of $\approx 80 \, \text{mrad}$. The radiation not coming from this zone is mainly originated in the compensator magnets and has a negligible intensity.

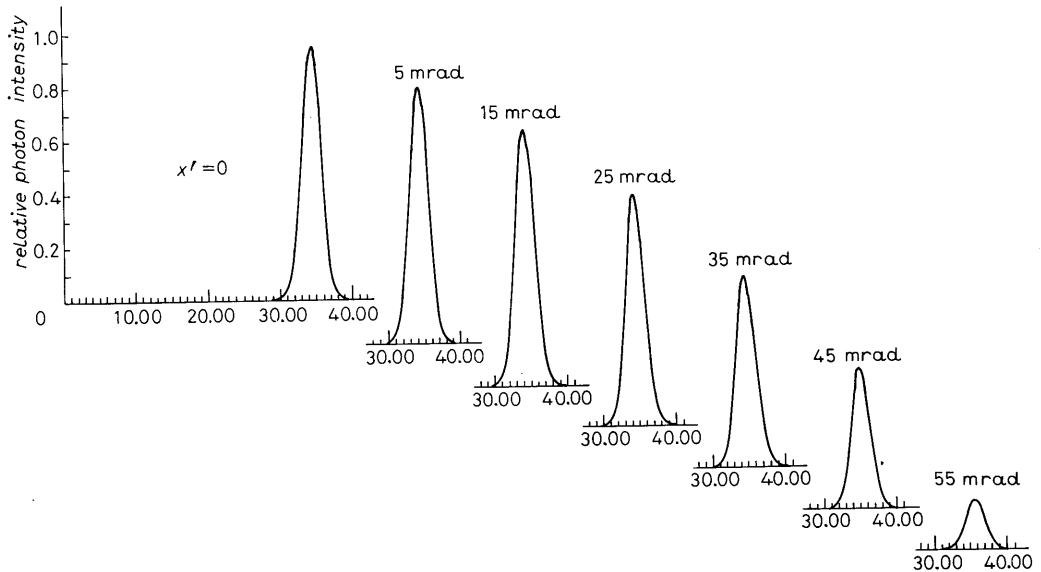Figure 9 shows in a more quantitative way the horizontal intensity distribution at different angles.

Fig. 9. – Cuts of the horizontal distribution of the radiation from the wiggler at different angles (arbitrary units).

3. – Effects of the superconducting wiggler on storage ring parameters.

The perturbation of the storage ring performance due to the introduction of the superconducting wiggler in the Adone lattice has been estimated from the calculated field map by integrating the electron trajectory through the central pole and the compensators.

Figure 2 shows the assumed field distribution and the resulting electron orbit, calculated with a numerical integration of the equation of motion.

The computer code evaluates also the synchrotron integrals (ref. [5]) under the assumption that the horizontal betatron function and the dispersion in the storage ring are not affected by the wiggler field: this assumption is essentially correct for the proposed system of central magnet and compensators, symmetrically designed with respect to a vertical plane through the axis of the storage ring straight section. From the synchrotron integrals the variation of the relevant radiation-dependent parameters can be calculated, and the results are summarized in table I.

In order to estimate the influence of the wiggler field on the linear lattice functions, the field distribution $B(s)$ has been simulated with rectangular sectors, as

TABLE I. – *Storage ring parameters at* 1.5 GeV.

|	Adone	Adone + SW
Radiated energy per turn (keV)	89.5	98.4
Horizontal betatron damping time (ms)	11.5	12.5
Vertical betatron damping time (ms)	11.7	10.7
Synchrotron damping time (ms)	6.0	5.0
Relative energy dispersion (%)	0.058	0.064
Horizontal emittance (mm·mrad)	0.24	0.41
Peak RF voltage for 100 h quantum lifetime (kV)	155.1	175.2
Relative energy acceptance (%)	0.38	0.41
Over voltage factor	1.73	1.78
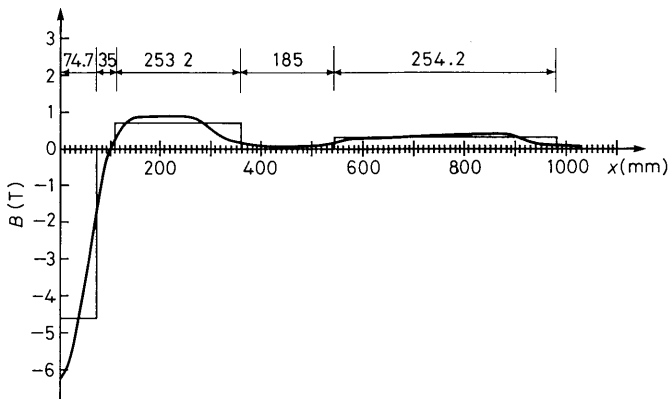
Fig. 10. – Simulation of the wiggler magnetic field with rectangular model.

shown in fig. 10. The lengths L_i and fields B_i of the sectors are determined by the system [6]

$$(3) \qquad B_i L_i = \int_i B(s) \, \mathrm{d}s \, ,$$

$$(4) \qquad B_i^2 L_i = \int_i B^2(s) \, \mathrm{d}s$$

and introduced in the input stream for the storage ring lattice for the CERN computer code MAD. The periodicity of the machine is reduced from 12 to 1 with a symmetry axis through the centre of the superconducting wiggler. The horizontal lattice functions (horizontal betatron and dispersion) are very weakly affected by the wiggler field, as expected from the horizontal symmetry of the magnet design, while the vertical betatron function changes significantly.

Figure 11 shows the behaviour of the vertical betatron function in one half of the ring (the second one is symmetric), compared with the same quantity without the wiggler.

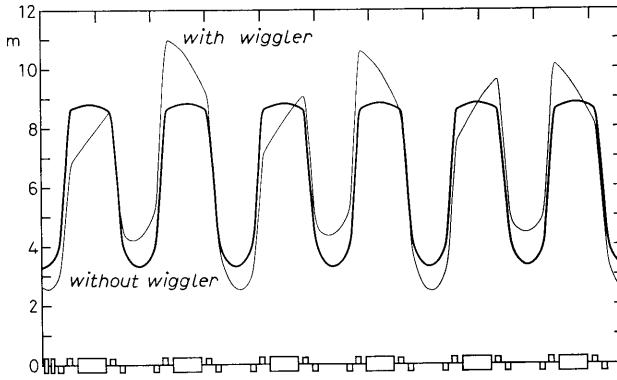Table II shows the variation of some optical parameters due to the wiggler.

Fig. 11. – Behaviour of the vertical β function in half-ring with and without the wiggler.

TABLE II. – *Optical parameters of Adone with and without the wiggler.*

	Adone	Adone + SW
Horizontal betatron wave number	3.100	3.100
Vertical betatron wave number	3.100	3.133
Horizontal chromaticity	− 3.146	− 3.146
Vertical chromaticity	− 3.871	− 4.052
Maximum horizontal betatron function (m)	9.18	9.18
Maximum vertical betatron function (m)	8.82	11.11
Maximum dispersion function (m)	2.05	2.05
Momentum compaction	0.067	0.067
R.m.s. horizontal beam size at wiggler (10% coupling) (mm)	1.72	2.10
R.m.s. vertical beam size at wiggler (10% coupling) (mm)	0.081	0.093
R.m.s. horizontal divergence at wiggler (10% coupling) (mrad)	0.47	0.61
R.m.s. vertical divergence at wiggler (10% coupling) (mrad)	0.025	0.036

4. – Electromagnetic design, superconducting cable choice. Power supply and controls. Quench protection.

4‘1. *Superconducting cable.* – To obtain the magnetic field profile shown in fig. 2, about 777 000 Amper-turns are needed for each coil. A good compromise between current and number of turns has been achieved choosing a superconducting cable having a $2 \cdot 1 \, \text{mm}^2$ rectangular cross-section: the Vacryflux 5001 manufactured by Vacuumschmelze.

The cable has 312 filaments of NbTi embedded in a high-conductivity copper matrix, it is electrically insulated with E-glass fibre and epoxy impregnated.

The main characteristics of this kind of cable are in table III.

TABLE III. – *Superconducting cable characteristics.*

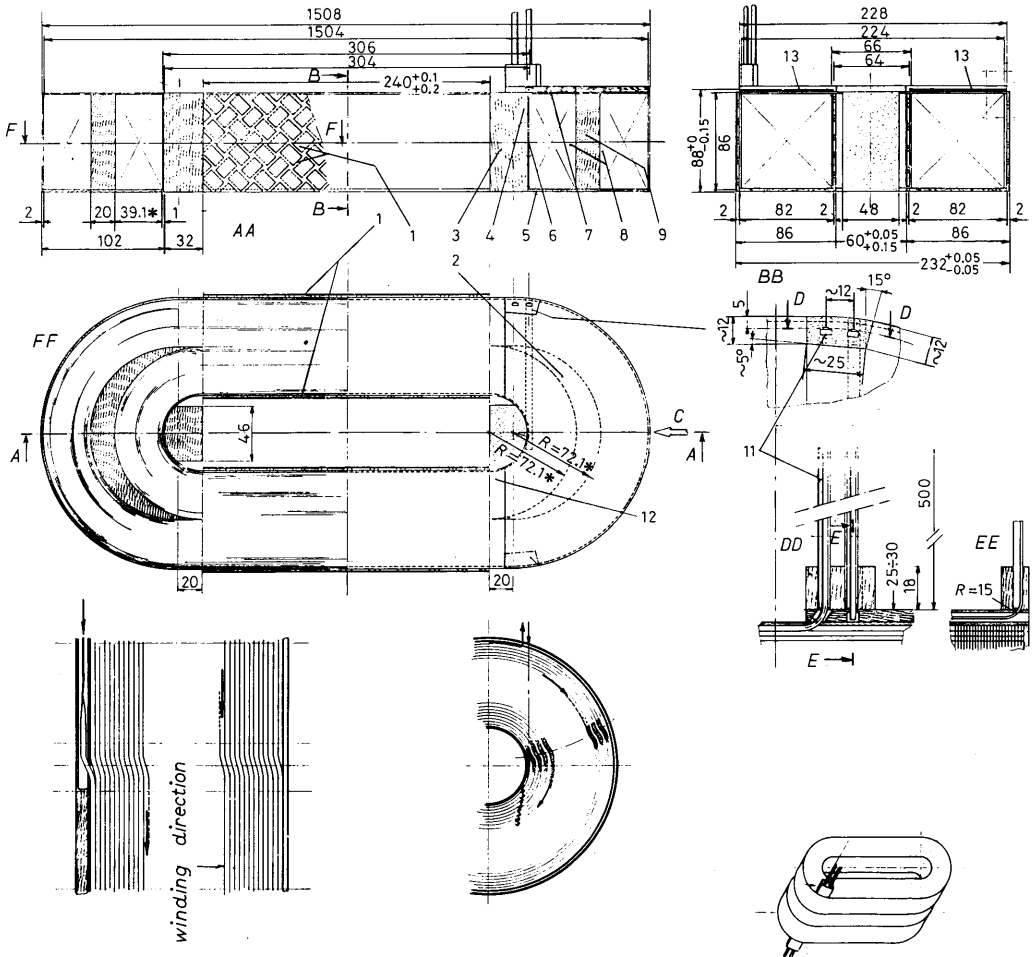|	Specified	Measured
Conductor cross-section:		
bare (mm^2)	2·1	$2^{+0.02} \cdot 1^{+0.016}_{-0.002}$
insulated (mm^2)		$2.234 \pm 0.004 \cdot 1.238^{+0.004}$
Twist pitch (mm)	50	—
Filament diameter (μm)	45	$45 + 1$
$\alpha = A\,Cu/A\,NbTi$	2.5 ± 0.4	$2.71^{+0.03}_{-0.04}$
Critical current (1 μV/cm):		
$B = 6\,T$ (A)		984 (4.2 K)
$B = 7\,T$ (A)		450 (4.6 K) ÷ 739.5 (4.2 K)
$B = 8\,T$ (A)		513 (4.2 K)
Cable weight (kg/km)		15

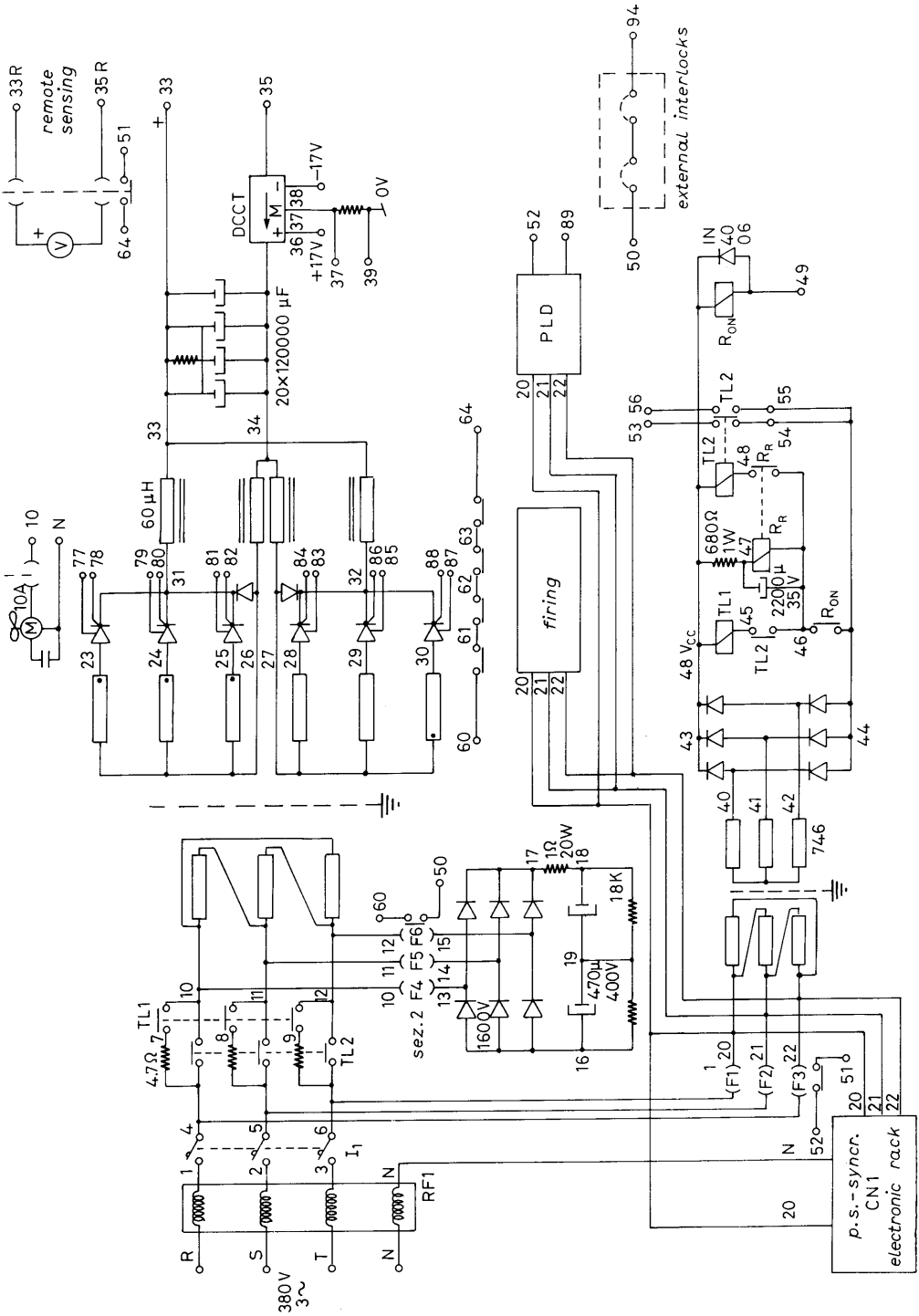Fig. 12. – General layout of the superconducting coil.

Fig. 13. – Electrical scheme of the power supply of the superconducting wiggler.

4˙2. *Superconducting coil.* – The race-track superconducting coil has a cross-section of $79 \cdot 83 \, mm^2$ and it is made up of 67 layers, 39 turns each. On the coil heads, the turns are thinned introducing an insulating separator, whose maximum thickness is 20 mm, avoiding too high magnetic field values in the points where the right part of the coil is bent, even if the tridimensional codes give a field less than 7 T at these points. Figure 12 shows the layout of the coil, the electrical characteristics of which are

Resistance	$26.78 \, \Omega$
Inductance	$1.22 H (1 \, kHz)$
Phase angle	89.2 deg.

4˙3. *Power supply.* – The power supply of the superconducting wiggler is a 10 V, 1000 A, SCR's regulated power supply having an internal interlock to avoid exceeding 400 A; it has a 0.1% current set point and a remote panel complete of commands and controls.

The power supply is made up of two three-phase star-connected bridges in parallel, on the current output a free-wheeling diode and a LC filter are mounted. A very high precision and stability DCCT warrants the current feedback. Such a kind of power supply has a stability and a ripple better than 0.01%. Figure 13 shows the layout of the power supply. An external stainless-steel resistance, 3 Ω, 120 kJ, (20 ÷ 120) °C, is in parallel between the output bars, allowing the discharge of the magnetic energy stored by the magnet during the quench.

4˙4. *Magnet excitation and quench.* – The quench detector is based on the differential reading of the coil voltage (see fig. 14), so that, if the quench arises, the
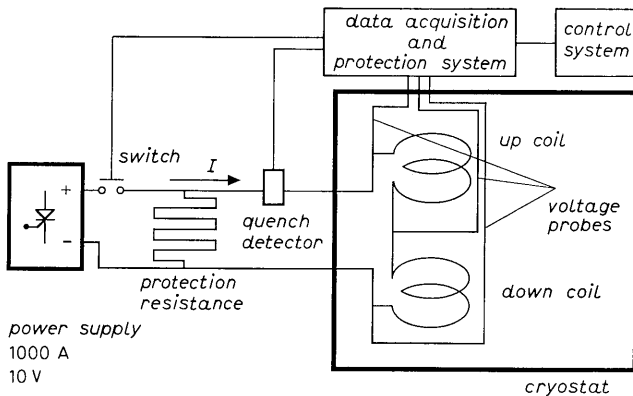

Fig. 14. – Protection sistem layout.

voltage asymmetry between one coil and the other is detected. After filtering, this signal is sent to a fast comparator and, if larger than a threshold, it activates an external breaker which disconnects the power supply. The same signal is also sent to an integrator, whose output is compared with a fixed threshold, and also this system, detecting long-term variations, activates the breaker. While the first system allows

detecting fast quenches, the second one, due to its better background rejection, can detect a low-speed transition phenomenon.

The electronics is realized with low drift operational amplifiers ($1\,\mu V/^\circ C$). A switch before the last actuator relay allows its exclusion during calibration and operation tests. An emergency button that commands directly the disconnection of the power supply completes the protection system.

The quenches were due mainly to

1) cracks into the epoxy,

2) coil and yoke mechanical settlement,

3) mechanical stress in a weak zone (the large race track coils are supported by the magnet yoke only over a short length of the long side but not at all at the curved heads).

In spite of the unfavourable arrangement only few transitions occured in the range 5.4 T to 6 T (see fig. 15). A maximum ramp of 0.6 A/s was used in the range from 0 to 290 A corresponding to a field of 5.560 T; above this value the ramp speed was reduced during training. The last quench occurred at 317.7 A, corresponding to (6.025 ± 0.003) T. The maximum current level was obtained by reducing the maximum ramp by a factor 10. Measurements on the field profile have been performed at different maximum field levels. The result is shown in fig. 16. No more quenches have been observed in the other excitations at any field level from 0 to 6 T. Increasing the bath temperature from 4.2 to 4.6 K no current limits were observed in the conductor.

The only way to obtain information about the propagation velocity of the hot spot was to perform voltage measurements at the coil terminals because no further leads were inserted. The expected voltage variation and the temperature increase at the nominal current value are shown in fig. 17 and 18[7]. Transient quantities are
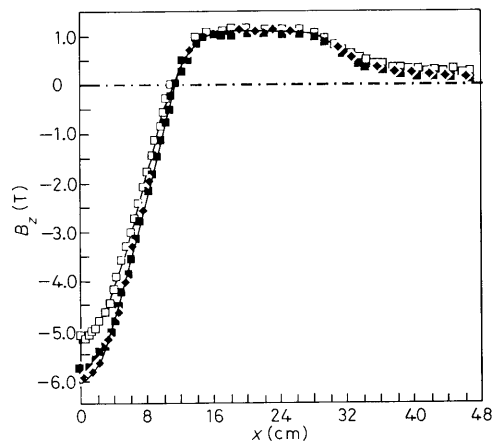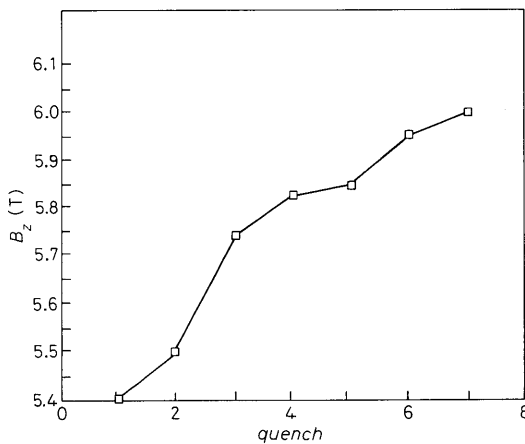

Fig. 15.   Fig. 16.

Fig. 15. – Magnet training.

Fig. 16. – Longitudinal field measurements. $B_{z\,\mathrm{max}}$(T): □ 5, ■ 6, ◆ 5.75.
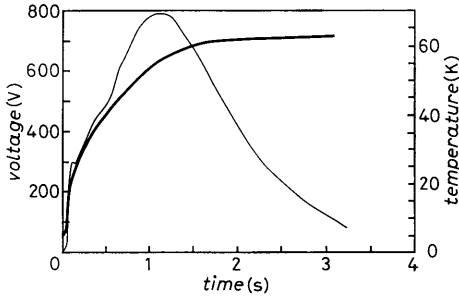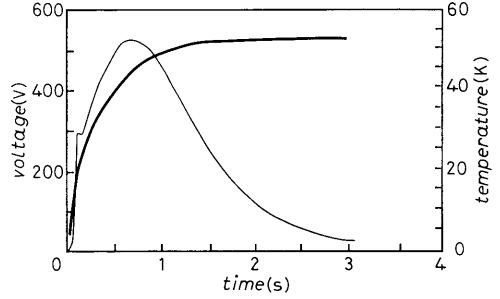
Fig. 17.

Fig. 17. – Voltage (——) and temperature (——) variation.

Fig. 18. – Voltage (——) and temperature (——) variation with a $3\,\Omega$ inserted resistor.

calculated with the following assumptions:

  1) the coil capacitance is neglected,

  2) the propagation velocity in the transverse plane is negligible compared to the velocity component in the longitudinal direction,

  3) a total $4\,H$ inductance is assumed.

  Figure 17 shows the behaviour without external protection and fig. 18 the same quantities with a $3\,\Omega$ protection resistor.

  The comparison of the normal zone resistance before switching on the external resistor with the computed values is shown in fig. 19.

  For the propagation velocity the best value to fit the experimental data is $0.9\,m/s$.

  Figure 20 shows the time behaviour of internal resistance at two different temperatures. Due to the increase of the velocity value it is clear that the slope of the
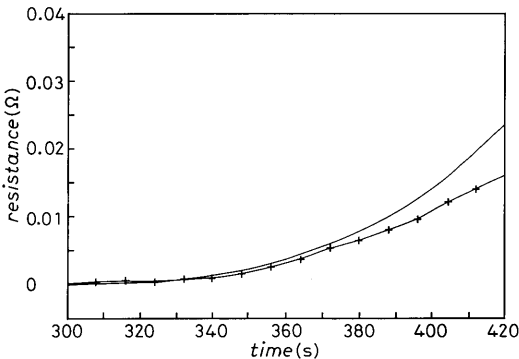

Fig. 19.

Fig. 20.

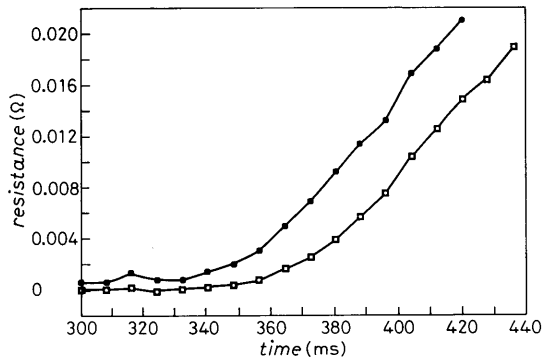Fig. 19. – Internal resistance behaviour before switching on the protection. + experimental, —— computed $(0.9\,m/s)$.

Fig. 20. – Internal resistance behaviour with external resistor. Temperature: □ 4.2, ■ 4.6.

resistance increases with the bath temperature. Other current measurements (after the insertion of the external resistor) have been carried on.

The comparison with the expected values using the same code but with some modification to take into account the real inductance of the coil is shown in fig. 21.
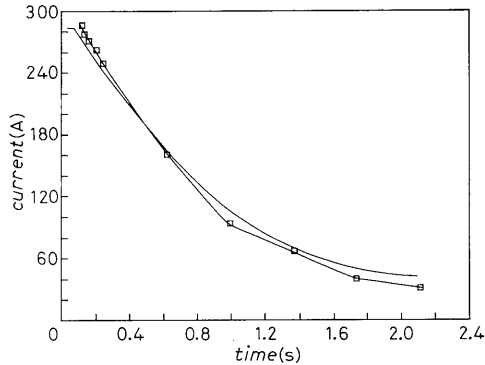

Fig. 21. – Current decay during a quench. □ experimental, —— computed $(V = 0.9\,\mathrm{ms}^{-1})$.

5. – Cryogenic design. Cryostat and helium liquefier/refrigerator characteristics.

5ʹ1. *Cryogenic system design.* – A cryogenic laboratory has been equipped to test the wiggler before its installation on Adone. A system consisting of a 1430 KPS liquefier, having a liquefaction capacity of 22 l/h and a refrigeration power of 60 W, has been installed in the laboratory. The cold box is connected with a 100 l stocking dewar through a 1.4 m horizontal cryogenic line. Two other transfer lines have been prepared to connect the refrigerator with the cryostat of the wiggler.

The laboratory is linked with a gas stocking area having a capacity of 1000 m³ of helium gas.

The compression system consists of

two compressors connected with the cold box by means of two lines, one at high pressure (16 atm), the second at low pressure (1 atm);

a vacuum system of rotaries pumps and a 1900 m³/h booster pump connected with the lines, one of which is designed to recover the helium gas evaporated during the quench;

a 30 m³ storage bag;

a four-stage recovery compressor to store the gas into the high-pressure (200 atm) gas bottles.

Figure 22 shows a pictorial view of the whole system.

A possible operation mode is shown in fig. 23, where a thermal dissipation of 20 W is assumed, a value very close to the whole static losses. As can be seen from fig. 24, showing the liquefaction capacity as a function of the refrigerating power, we can obtain 20 W using only one compressor but without liquid helium production.

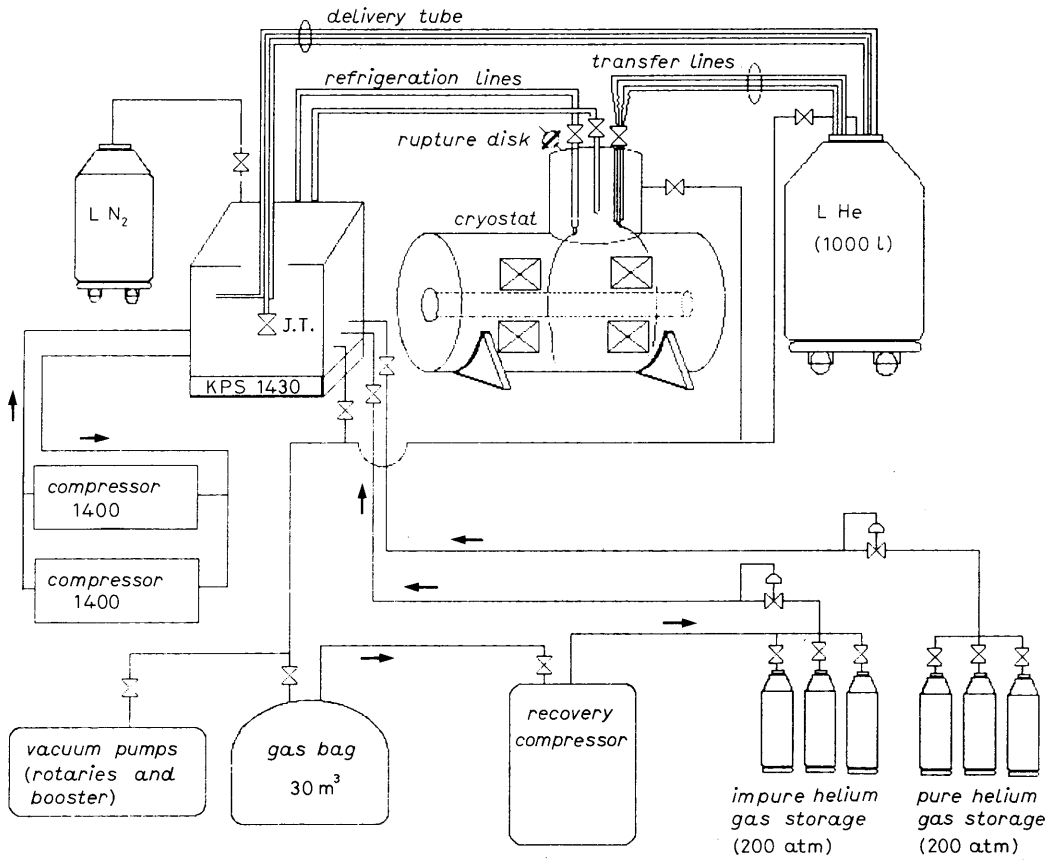The temperature of liquid helium coming back to the liquefier is 4.6 K and its

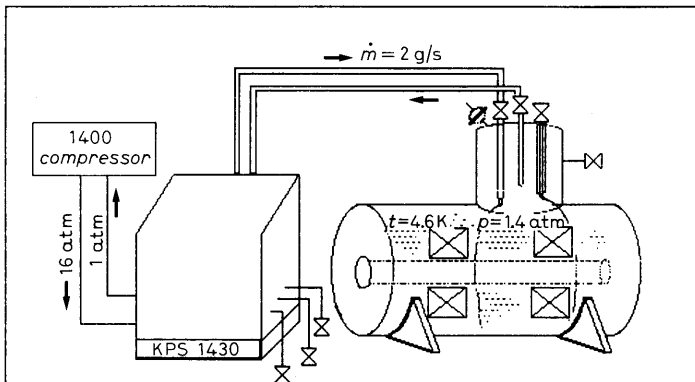Fig. 22. – General view of the laboratory cryogenic system.

Fig. 23. – Schematic view of the cryogenic system powering the wiggler after its installation on Adone.
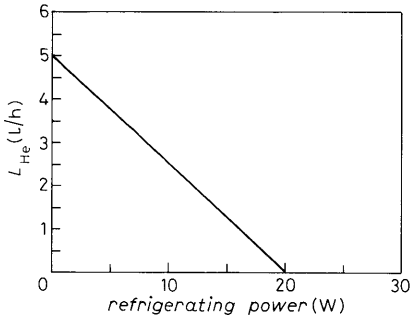
Fig. 24.   Fig. 25.

Fig. 24. – Liquefaction capacity as a function of the refrigerating power.
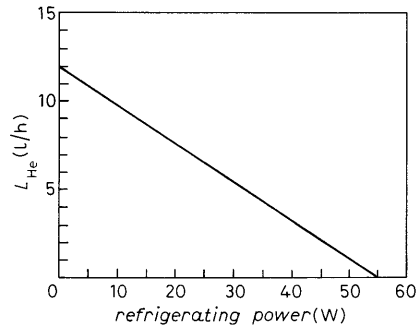
Fig. 25. – Liquefaction capacity as a function of the refrigerating power for a screw compressor.

over-pressure is 280 mbar. We have estimated that the helium flux returning to the cold box is 2 g/s and its temperature reaches 19 K. If the first heat exchanger into the cold box is cooled by liquid nitrogen, the power can be increased by 25%, with a flux of 2.5 g/s. Once the steady state has been reached, the pressure oscillations are of the order of 1% so that the equilibrium temperature is stable at this level.

After the installation of the wiggler on the storage ring, the superconducting coils will be cooled by means of a simpler system consisting of the 1430 cold box and a screw compressor.

The cryogenic losses of the system will be compensated by the on-line refrigerator, these losses are due to the cryostat and cryogenic line static dissipation and also to the current leads.

A dewar can be added to the system, as a heat tank, to speed up the first cooling and to hold the liquified helium. In fact, if the refrigeration power exceeds the needs, the system will work on a point of the line shown in fig. 25, where the helium liquefaction capacity of a screw compressor is reported as a function of the refrigeration power.

5'2. *Cryostat design*. – Since the two s.c. coils together with the two yokes and the central plate are cooled by boiling helium at 4.6 K, the cryostat has been designed in such a way to fit these requirements.

A transverse cross-section of the cryo-magnetic system is shown in fig. 26; the main cryostat components are the external vessel, the helium vessel, the radiation screen, the service turret.

The external vessel has a cylindrical shape and it is made in austenitic stainless steel AISI 304L; it can withstand the pressure occurring during testing and operation of the magnet. Its rupture pressure is 40 atm; the lateral flanges are sealed by «O ring» elastomers. The vessel permits a sequential assembly around the magnet allowing easy testing and repair of welded joints.

The helium vessel is made of stainless-steel AISI 316L and it consists of a cylindrical shell closed by flat end covers TIG welded; the measured leak rate is 10^{-12} Torr l/s.
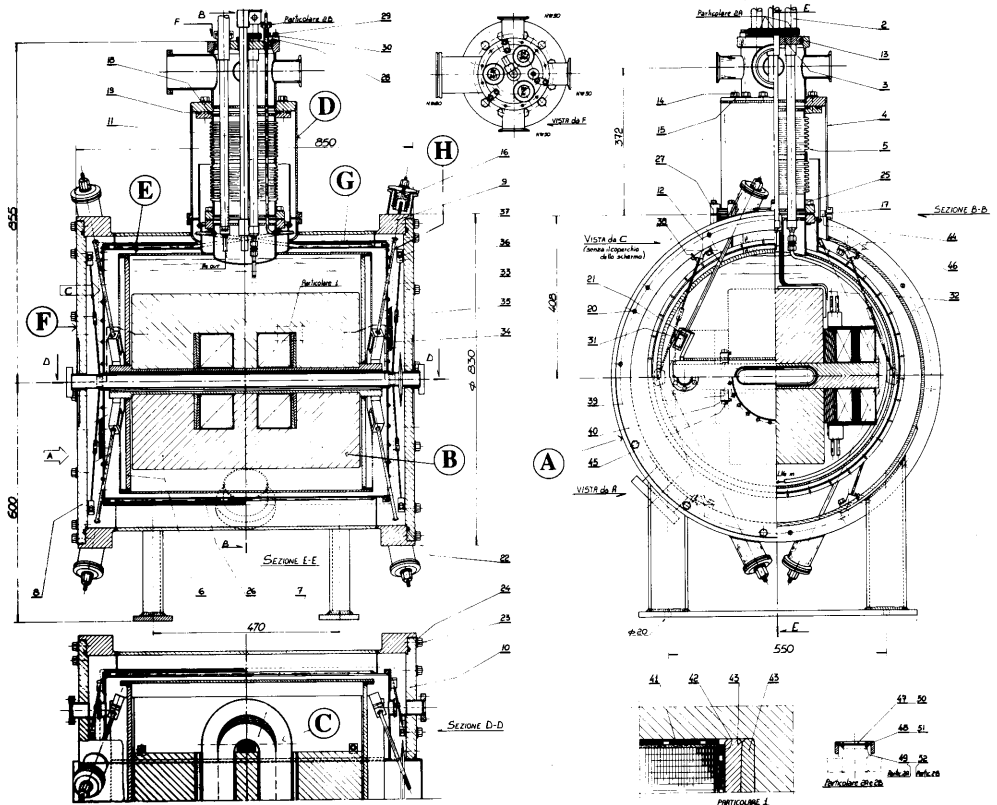
Fig. 26. – Transverse cross-section of the cryomagnet. A: external vessel, B: magnetic yokes, C: SC coils, D: service turret, E: helium vessel, F: flanges, G: radiation screen, H: suspension rods.

The radiation screen is made by copper OFHC, it incorporates a cooling circuit in which the boil-off vapour from the helium bath flows. Its calculated and measured average temperature is 80 K. The end plates of the screen are cooled by conduction; the screen is wrapped with 50 layers of aluminized mylar super-insulation, crinkled. After degassing the initial vacuum of 10^{-4} Torr is improved by cryo-pumping up to 10^{-7} Torr.

The magnet, whose mass is 356 kg, is suspended at its quarter points by 8 tension rods made of titanium alloy to reduce the heat leak at 0.1 W.

The service turret is located on the neck of the cryostat to allow the current leads to transport the current to the s.c. coils. On top of the turret there is a flange with three bayonet attacks for the helium transfer lines, two of which link the refrigerator cold box to the cryostat and one to a 1000 l dewar buffer to be used in case of electrical power failure. The calculated heat leak for such attacks is 1 W/bayonet. In order to limit the heat inleak to the helium bath and avoid excessive cooling of the terminal flange, which could result in condensation or icing, two baffles are mounted inside the turret.

The breakdown for the major heat leaks is shown in the table here below:

Radiation from heat screen	3 W (calculated)
Conduction along the suspension rods	0.1 W (calculated)
Warm bore	0.75 W
Helium vessel	0.102 W
Service turret with current leads at 400 A	0.8 W
Others	1.16 W
Total	5.9 W (calculated)

The total losses have been measured during a test made at Ansaldo, where the magnet has been cooled by means of the dewars, their value is 5000 Nl/h equivalent to 4.6 W.
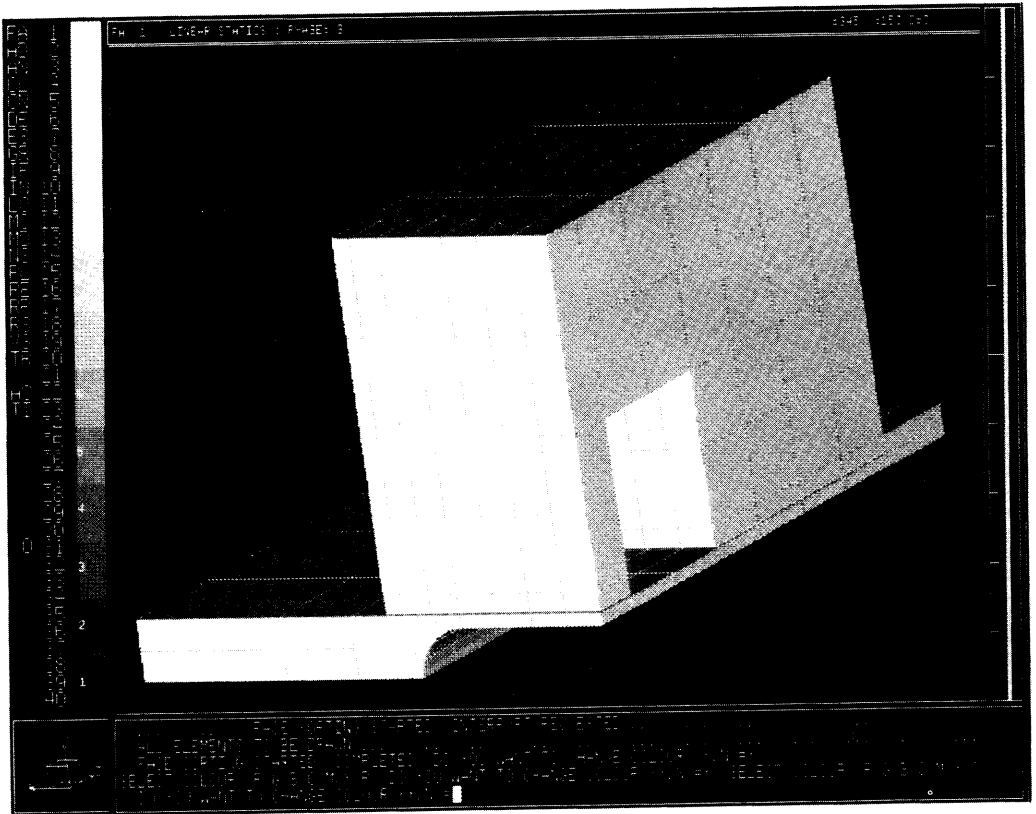

Fig. 27. – Shading view of the finite element subdivision of the yoke and the central plate.

6. = Mechanical design. Finite element method structural analysis of the most critical parts.

Stresses and strains of the central plate of the magnet have been studied with the code PAFEC version 7.1.
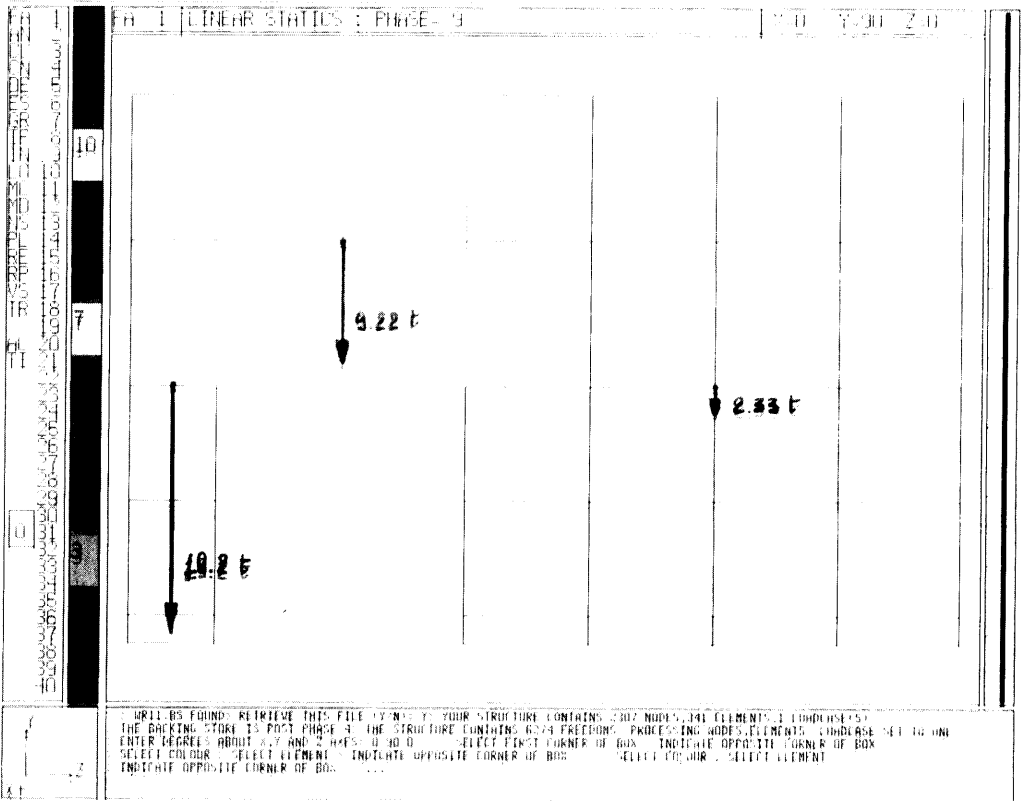
Only 1/8 of the complete magnet (fig. 27) has been studied, but suitable constraints have been assigned to the three symmetry planes parallel to the axes.

The magnetic attractive force has been differently distributed on the three iron regions (fig. 28) overhanging the gap of each half magnet, namely the pole, the iron zone over the superconducting coil and the shield. To do that, different fictitious densities have been fixed for the three regions in order to obtain the same values of the vertical forces that the TOSCA code, used by Ansaldo, has predicted.

Three cases have been studied: a) structural continuity between the iron of the magnetic yoke and the central plate; b) structural discontinuity between yoke and plate: the two parts can glide on their contact planes hindered by friction; c) as in b) but adding the lateral force due to the coil and, since it is not possible to evaluate which fraction of the force is absorbed by the coil rigidity, it has been entirely applied

like a uniform pressure on the side of the shield. The value of this pressure, calculated by means of Poisson, is $1.911 \cdot 10^7 \, \text{N}/\text{m}^2$.

The densities of the three iron regions are

pole	$7.092 \cdot 10^6 \, \text{kg}_{\text{mass}}/\text{m}^3$
iron overhanging the coil	$4.467 \cdot 10^6 \, \text{kg}_{\text{mass}}/\text{m}^3$
shield	$0.300 \cdot 10^6 \, \text{kg}_{\text{mass}}/\text{m}^3$
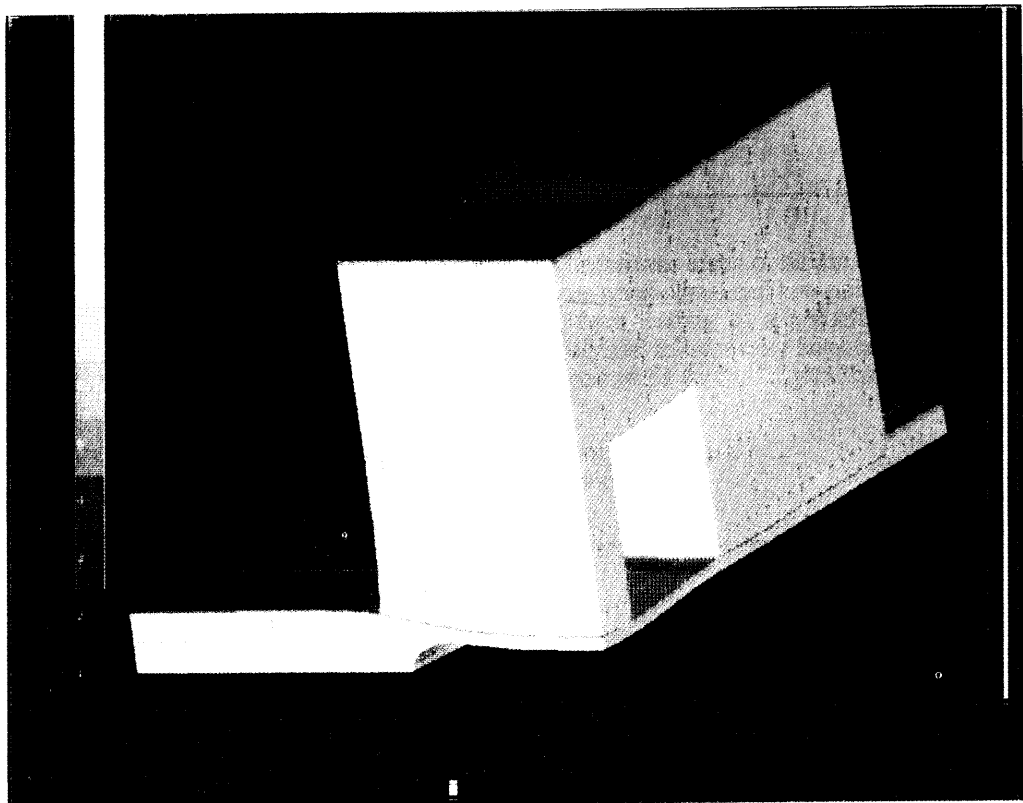
Fig. 29. – Deformation with structural continuity.

The adopted Young moduli of the materials are

iron	$1.95 \cdot 10^{11} \, \text{N}/\text{m}^2$
steel	$2.09 \cdot 10^{11} \, \text{N}/\text{m}^2$.

The code calculations show that the assumption of structural continuity between the yoke and the central plate leads to optimistic results and that the lateral force due to the coil makes the situation worse. In any case the maximum stress, evaluated according to Von Mises, can be tolerated by the material. The following values are

obtained:

with structural continuity	$10.2 \, \mathrm{kg/mm^2}$
without structural continuity	$12.3 \, \mathrm{kg/mm^2}$
without structural continuity and with lateral force	$19.6 \, \mathrm{kg/mm^2}$

The maximum displacement of the central zone of the plate is

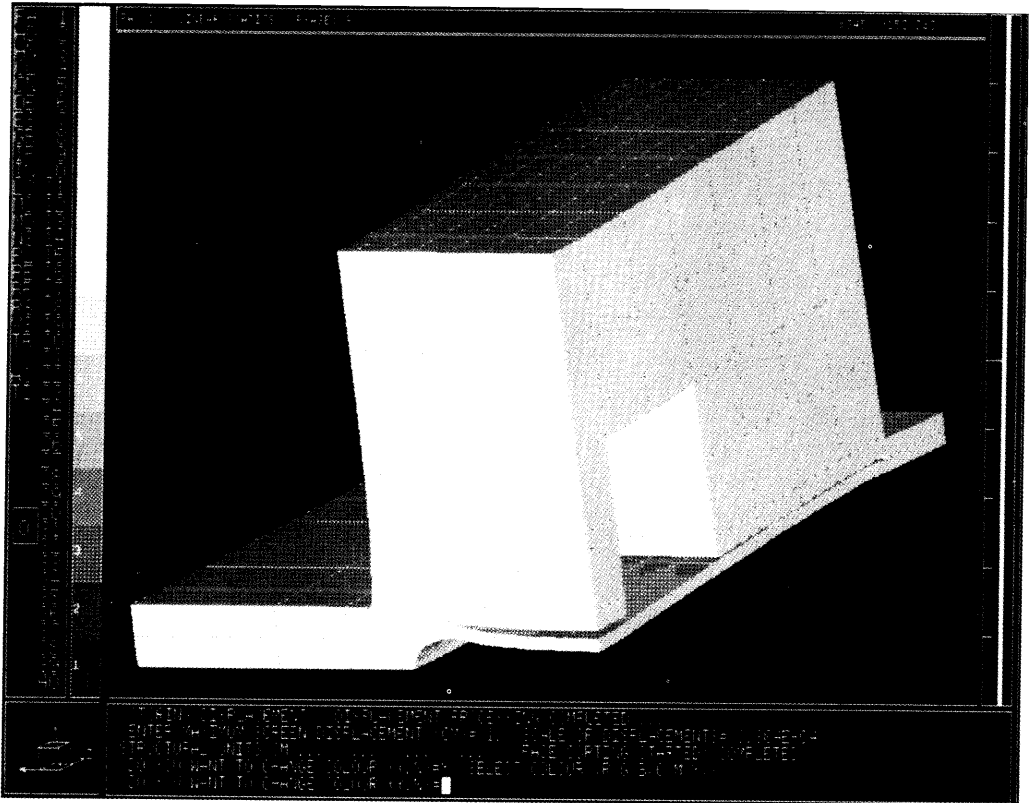|	
with structural continuity	$0.2 \, \mathrm{mm}$
without structural continuity	$0.4 \, \mathrm{mm}$
without structural continuity and with lateral force	$0.6 \, \mathrm{mm}$

Fig. 30. – Deformation without structural continuity.

The difference between the first case and the second one depends on the rigidity transmitted to the central plate by the magnetic yoke: the structural continuity allows a more favourable stress distribution into the plate.

The difference between the second and the third case is due to the combination of two effects:

the lateral force, raising the shield, determines a bad stress distribution on the central part of the plate;

since the shield is blocked at the plate end, a longitudinal stress is induced and it is added to that produced by the attractive force between the two magnetic yokes.

The real situation can be thought as an intermediate scheme between the second and third case studied. Figures 29-31 show the deformation concerning all the cases taken into account, while fig. 32-34 show the Von Mises stress distribution.
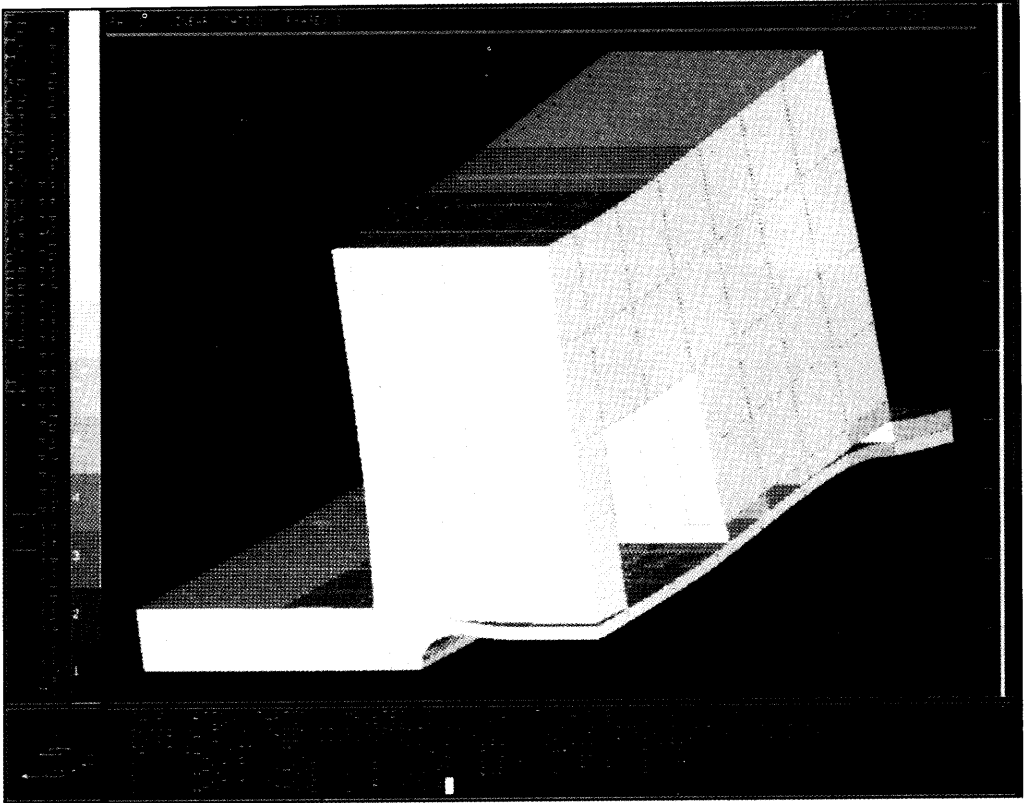
Fig. 31. – Deformation without structural continuity and with the lateral force.

7. – Compensation magnet design.

The condition $\int B_z \, dl = 0$ along the beam direction is satisfied by two compensator magnets placed before and after the superconducting pole. Figure 3 shows clearly that the integral of the magnetic field due to the shields does not entirely compensate sthe field integral of the 6 T superconducting pole, because of the lateral flux dispersion. The missing part must be supplied by means of two compensator

magnets, since the experimental requirement of a single light spot does not allow to increase the positive value of the magnetic field.

The magnet design has taken into account this requirement so that the maximum field is of the same order of magnitude of the shield one. The compatibility with the cryostat size and the Adone straight section has enforced a mechanical length of 0.33 m and a magnetic field of 0.57 T. In order to avoid quadrupole gradients, a H configuration has been chosen for the magnets, with a pole length/gap ratio of 4. Table IV summarizes the main parameters of the compensator magnets.
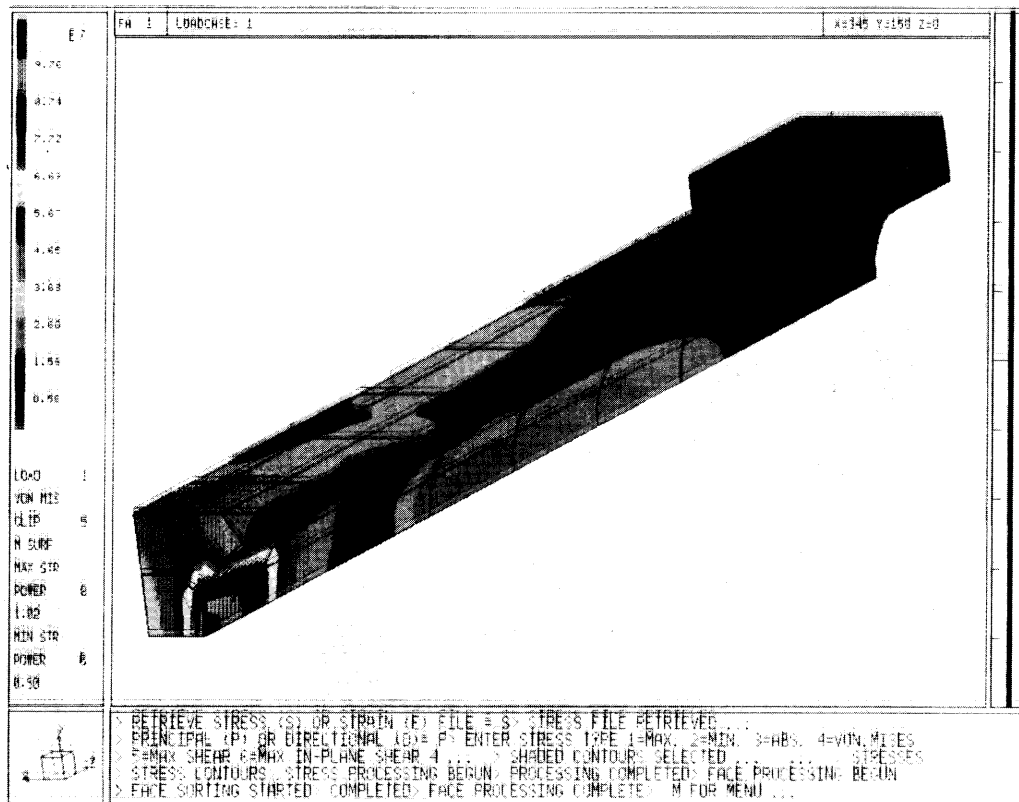

Fig. 32. – Von Mises's stress distribution in the critical part of the central plate (first case).

The magnetic field profile has been studied by means of the bidimensional code Magnet. Two 1 cm wide, stepped lateral shims have been added to obtain a larger useful zone. The thickness of the shims is 0.5 mm for the first and 1.2 mm for the second step. A preliminary measurement, with 340 A current, gave a field value of 3040 Gauss in comparison with 3065 Gauss predicted by the code. In the transverse direction there is a variation of $\pm 0.1\%$ within $(-7.3 \div +7.15)$ cm with respect to the pole centre. Figure 35 shows the measured and calculated values corresponding to
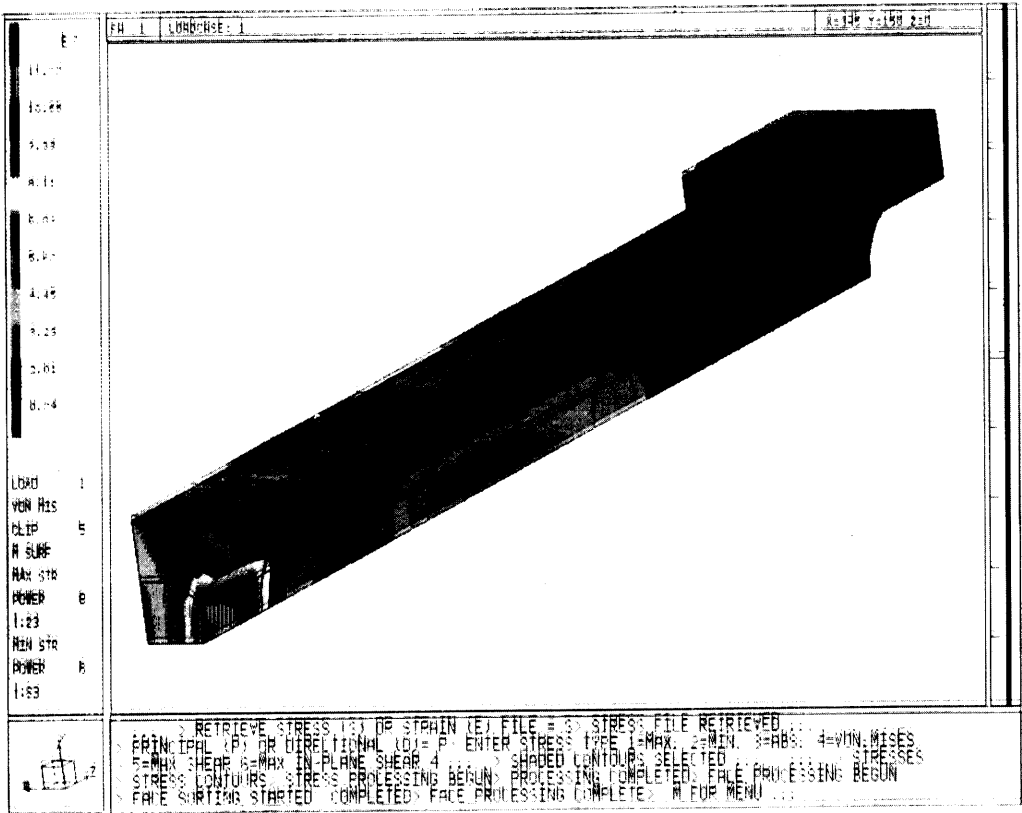
Fig. 38. – Von Mises's stress distribution in the critical part of the central plate (second case).

340 A. Figure 36 shows the field along the beam direction giving the magnetic half-length of the compensator magnet.

If the sextupole field term introduced by the wiggler has to be corrected, the compensator pole surfaces can be machined so that a sextupole term having the opposite slope is obtained. This can be done taking into account that the equipotential surface describing the sum of a dipole field B_0 with a sextupole having sextupole constant S [8] is given by

(5) $$y = \{[x_0/kx] - [x_0^3/3x] + [x^2/3] - 1/k\}^{1/2} ,$$

where

$$x_0 = \text{half-gap} ,$$

$$k = S/B_0 ,$$

$$x = \text{transverse coordinate} ,$$
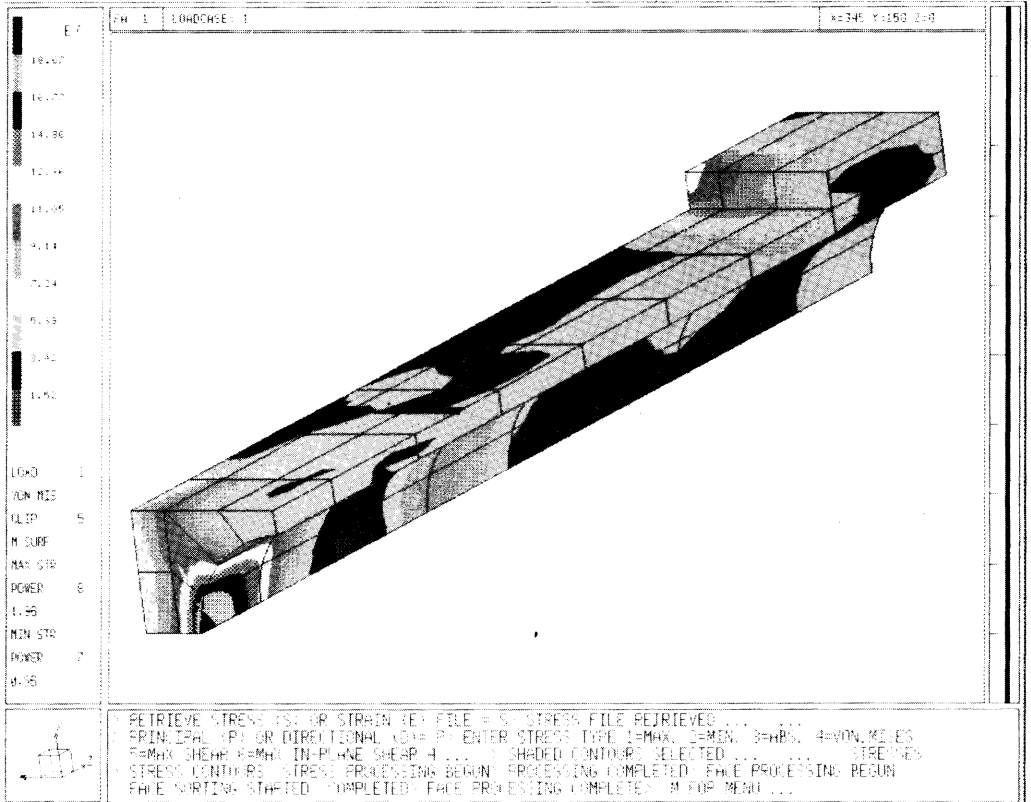
$$y = \text{vertical coordinate} .$$

Fig. 34. – Von Mises's stress distribution in the critical part of the central plate (third case).

TABLE IV. – *Compensator magnets main parameters list.*

Gap	50	mm
Pole width	200	mm
Return leg width	70 ($\cdot$2)	mm
Nominal field on axis	5.74	kG
Maximum field on axis	8.5	kG
Number of coils	2	—
Nominal ampere-turns per coil	11474	A-turn
Maximum ampere-turns per coil	18000	A-turn
Nominal current density	16.35	A/mm^2
Maximum current density	25.65	A/mm^2
Number of turns per coil	18	—
Conductor: copper	8$\cdot$8$\oslash$5	mm^2
Useful conductor area	39	mm^2
Nominal current	637.5	A
Maximum current	1000	A
Nominal power per magnet	8.9	kW
Maximum power per magnet	22.0	kW
Nominal voltage	14	V
Maximum voltage	22	V
Magnet resistence	0.022	Ω
Magnet inductance	2.6	mH

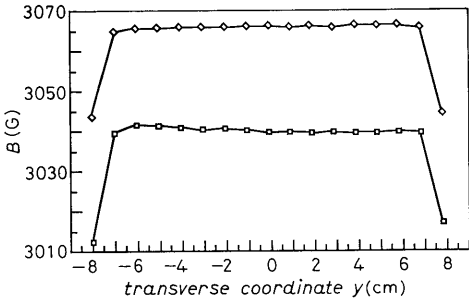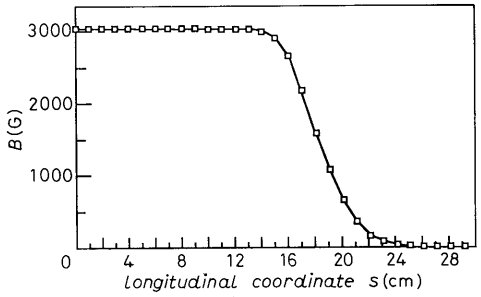Fig. 35.   Fig. 36.

Fig. 35. – Measured (□) and calculated (◇) magnetic-field profile of the compensator magnets.

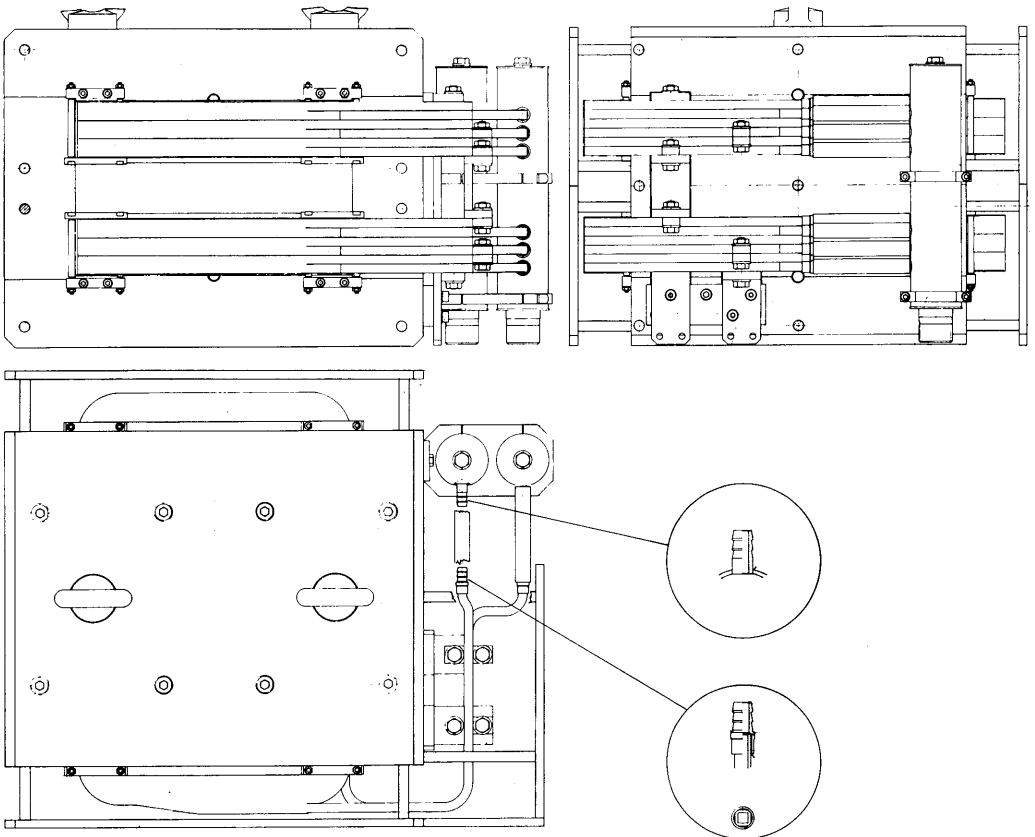Fig. 36. – Magnetic half-length of the compensator magnets.

Fig. 37. – Mechanical layout of the compensator magnets.

Figure 37 shows the mechanical layout of the compensator magnets realized with Armco iron. Two power supplies, $(0 \div 22)\,$V, $(0 \div 1000)\,$A, have been designed and built. They are SCR's controlled; two six-phase bridges in parallel with a LC filter on the output give a 600 Hz ripple of the order of 10^{-4}; the stability is made of the same order by means of a precise DCCT.

The coils are water cooled and the measured ΔT at the maximum power with a water flow of $1.25\,\text{m}^3$/h is about 13 °C.

8. – Magnetic measurement system design. Flip coils and Hall probe actuators design. Dedicated data acquisition system.

In order to measure the superconducting wiggler, two kinds of magnetic measurements will be carried out:

point-to-point magnetic-field map on the horizontal plane simmetry,

magnetic-field integral measurement along the magnet axis.

Hall probes will be used for the point-to-point maps, while an integrator magnetometer with a small rotating coil as sensitive element will be used to measure the fringe field and the 6 T field peak.

We will make use of a long rotating coil to measure the field integral and its integrated multipolar components.

Integrator magnetometer: this instrument has a small coil rotated manually in a magnetic field and an integrator realized with very high stabilized integrating circuits. The coil has a 5 mm diameter and is 5 mm high, giving an accuracy of 0.5% full scale, three ranges (200 mT, 2 T, 20 T). The thermal drift, after two hours, is less than 0.02 mT per minute. The instrument has been realized by Magnex (Abingdon, UK).

Hall generators: for the point-to-point magnetic field map, the Hall probes made by Lake Shore Cryotronics, having a maximum linearity error of $\pm 1\%$ in the range $\pm 3\,$T, and $\pm 2\%$ in $\pm 15\,$T, will be employed. The magnetic sensitivity is 0.8 mV/kG.

The circular sensitive area has 1 mm diameter in the planar type and 0.5 mm diameter in the axial type.

Hall probe coordinatometer: this system has been built by Contek (Varallo, Italy), it consists of a carriage pneumatically suspended in a reference guide box. A bronze ribbon moves the carriage carrying the Hall plates and an encoder reads the probe longitudinal position during field mapping. The probe can be manually moved laterally and vertically on the carriage to measure magnetic-field maps outside the system axis. Longitudinal position can be reproduced within 20 µm. The error on the vertical and horizontal position of the Hall probe, due to the reference box deflection, is less than 3/10 mm. The system may be improved with an optical telescope to measure the absolute position of the Hall probe.

Integrated magnetic-field measurements: the magnetic-field integral along the beam trajectory can be expanded as

$$(6) \qquad \int B \, \mathrm{d}s = C + Gz + Hz^2 + Mz^3 + \dots ,$$

where

s = longitudinal coordinate	z = transverse coordinate
C = dipole term	G = quadrupole term
H = sextupole term	M = octupole term.

The dipole term can be neglected since the condition of vanishing integral is fulfilled on axis by means of the compensator magnets, while for G, H, M there are upper limits to be compatible with the storage ring lattice. These limits are $G \leqslant 0.75\,\mathrm{G}$, $H \leqslant 0.75\,\mathrm{G/m}$, $M \leqslant 1\,\mathrm{G/m^2}$. C must be less than $1\,\mathrm{G \cdot m}$. What we want to do with the long rotating coil is to make the magnetic-field integral vanish on the ideal axis of the beam, then move the LRC along the transverse coordinate to measure $\int B\,ds = f(z)$. These values will be plotted and the best fit of the obtained curve will give the values of G, H, M. The most important of these coefficients is H, because G should vanish because of the system symmetry and M is expected to be very small. If necessary the sextupole term introduced by the wiggler can be compensated by machining the pole profile of the compensator magnets.

Long rotating coil: LRC consists of a 3 m long coil wound onto a nonconducting former (tufnol) 20 mm in diameter. The main LRC parameters are listed in table V.

TABLE V. – *Main parameters of the long rotating coil.*

Wire type	copper 38 swg	0.152 mm dia.
No. of turns, N	494	—
Diameter of former	20	mm
Length of former	3000	mm
Winding groove size	4·4	mm^2
Turns density	30.9	turns per mm^2
Former material	Tufnol type 6F/45	
Centre-to-centre distance between wire turns (d)	15.6	mm
Nd	7.7	m
V_{max} (at 1 Hz)	$7.7 \cdot 2 \cdot \pi \cdot 10^{-3} \equiv 0.484$	mV

The coil is impregnated with epoxy resin to hold turns rigidly during rotation and the whole coil assembly is contained within a 3 part precision glass tube. The joint between the three glass tubes occurs at a distance of 425 mm from the nominal centre of the coil.

At the position of the joint in the glass additional supports are provided on movable horizontal tables. The tube is supported at its ends and driven at one of them by a master «rotate/translate» stepper motor drive and at the other by a slave translation stepper motor drive.

Figure 38 shows the system during the acceptance tests.

The stepper motor moves the flip coil rotationally around the longitudinal axis; the rotation may be by fixed angles (180°, 360°, etc.) or continuously at a frequency from 0 to 10 Hz. The translational movement in the transverse direction can be performed up to ± 5 cm from the central axis of the magnet.
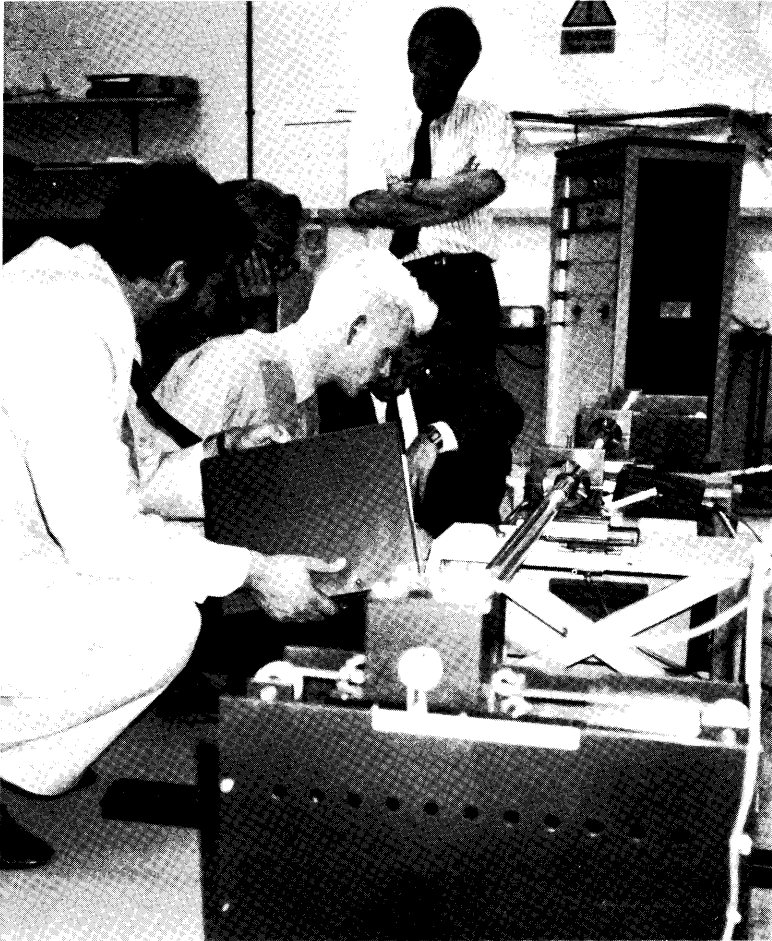
Fig. 38. – Long rotating coil during the acceptance tests.

The control system consists of modular components as follows:

   a) 1 rotation stepper motor,

   b) 2 translate stepper motors,

   c) stepper motor drive CD 20 rotate,

   d) 2 stepper motor drive CD 20 translate,

   e) power supply module,

   f) MC1 indexer,

   g) MC3 sequencer,

   h) MC2 clock/datum,

   i) Rev counter.

The CD 20 stepper motor drives provide the pulses for the motor windings, and the pulse rate is derived from the MC2 clock card. The two CD 20 drives for translation are driven from the same clock pulses and so the two stepper motors act together.

The indexer and sequencer cards provide controlling start and stop to the motor. Motor start-up requires an acceleration period during which the motor reaches full speed, this is pre-set and depends on the required torque. The indexer and sequencer can also count the steps fed to the motors and stop it after a pre-determined number, or when the data are received.

The sequencer card can have pre-programmed activities set up so that a number of repetitive actions can be performed. There are three possible modes of operation. «Manual», «Set-up» and «Programmed».

Table VI shows the figures concerning linearity during the rotation and after a translation; the deviation is within ± 0.5 mm.

The sensitivity of the system has been measured with no external field to measure the vertical component of the earth magnetic field. We have found 0.43 G, which is in very good agreement with another similar measure made at CERN (0.42 G - Lep Note 593).

More tests, including the s.c. wiggler and the compensating magnets, will be available in next future.

The Data Acquisition and Control system 3852A made by Hewlett & Packard, with the 20 Mbytes hard disk, microfloppy, plotter and writer is ready to begin the acquisition of the field values.

The HP 3457A multimeter, 7 1/2 digits, will be used to measure the Hall voltages and the signals from the long rotating coil induced by the magnetic field.

TABLE VI. – *Deflection of the long rotating coil during rotation and translation.*

Rotate continuous deviation centre section	± 0.202	mm
Pick-up end section	± 0.381	mm
Motor end section	± 0.20	mm
Translate to + 2.5 cm		
Rotate continuous deviation centre section	± 0.20	mm
Pick-up end section	± 0.38	mm
Motor end section	± 0.20	mm
Translate to + 5.0 cm		
Rotate continuous deviation centre section	± 0.20	mm
Pick-up end section	± 0.38	mm
Motor end section	± 0.20	mm
Translate to − 2.5 cm		
Rotate continuous deviation centre section	± 0.20	mm
Pick-up end section	± 0.38	mm
Motor end section	± 0.20	mm
Translate to − 5.0 cm		
Rotate continuous deviation centre section	± 0.20	mm
Pick-up end section	± 0.38	mm
Motor end section	± 0.20	mm

9. – Wiggler alignment and position control.

The wiggler alignment on the storage ring straight section should fulfill the following requirements:

1) the particle orbit in the Wiggler should match the ideal orbit in the ring, so that it stays unchanged outside the wiggler straight section;

2) the Wiggler magnetic symmetry plane should be horizontal so that the particle orbit in the wiggler lies in the same plane of the unperturbed storage ring orbit;

3) both entrance and exit points and the magnetic symmetry plane should be referenced outside the cryostat by optical targets, suitable for alignment operation;

4) the alignment accuracy should be the same of any other magnetic component of the machine, namely better than ± 0.1 mm.

To achieve this goal, the mechanical assembling accuracy in terms of positioning and centring of the magnetic poles on the stainless-steel supporting central plate was
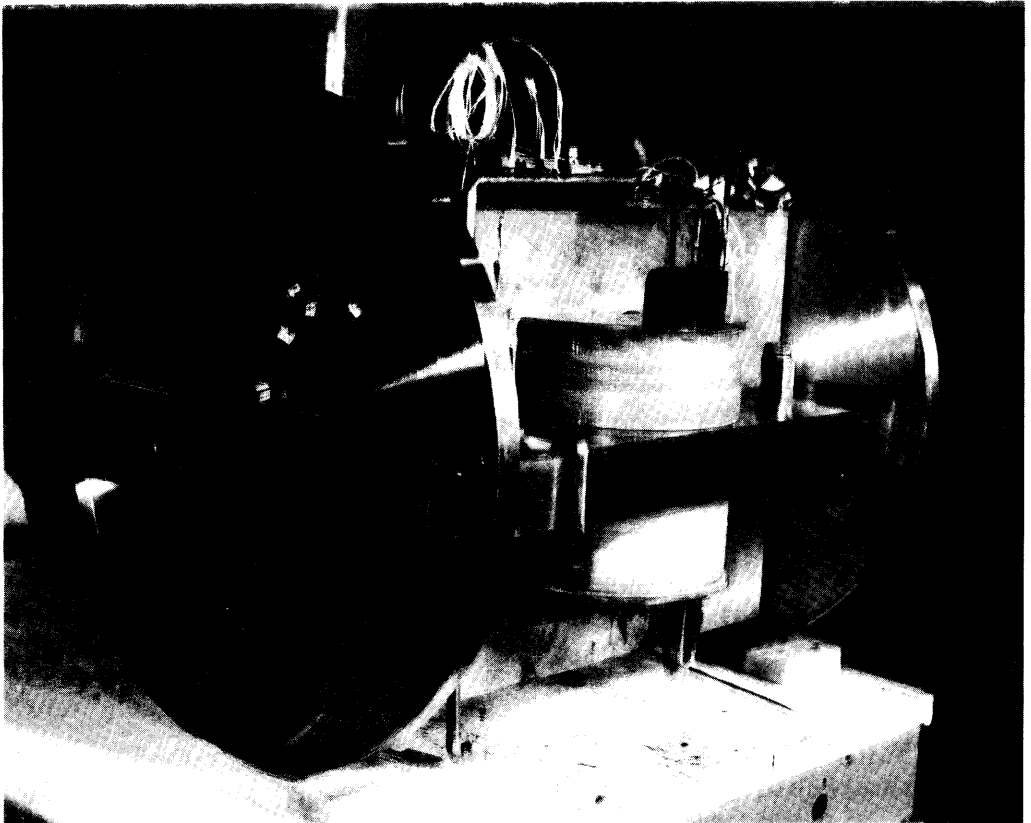

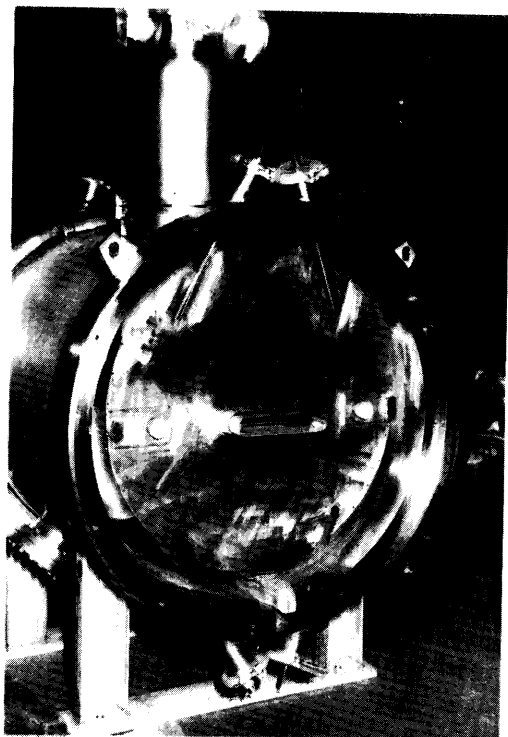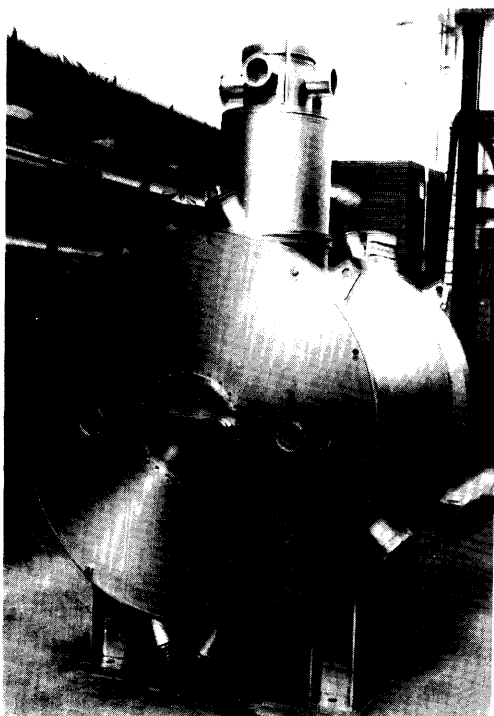Fig. 39. – Helium vessel end plates welded to the central plate.

Fig. 40.   Fig. 41.

Fig. 40. – External vessel end plate with view ports.

Fig. 41. – Radiation shield end plate with holes (blanked during the assembling).

performed within ± 0.05 mm and an even higher precision was prescribed in terms of machining the surfaces of the cold part.

Great attention was paid in achieving the parallelism of planes, flanges and centre lines so that the final turning and milling operations of the helium container end plates were made after welding them to the central plate (see fig. 39). By this way every possible distortion effect due to the welding shrinkage was avoided.

After the precise construction and assembling of the magnet cold parts described above, the stainless-steel supporting central plate to which the poles and coils are anchored has been marked off at both ends in order to reference the magnet horizontal symmetry axis. This operation, performed with very high precision, allowed the creation of two fiducial reference targets at both helium vessel end plates. Obviously the centre line between the fiducial marks represents the cryostat axis which must be positioned on the Adone straight section axis.

The final problem to be solved is how to see from outside the cryostat the above-described alignment marks. As is well known the helium container is surrounded by the radiation shield with superinsulation and the whole is included into the cryostat external vessel, the vacuum container. Once the latter is closed no access is possible to the radiation shield, nor to the helium vessel. The solution to be adopted should avoid increasing heat leaks.
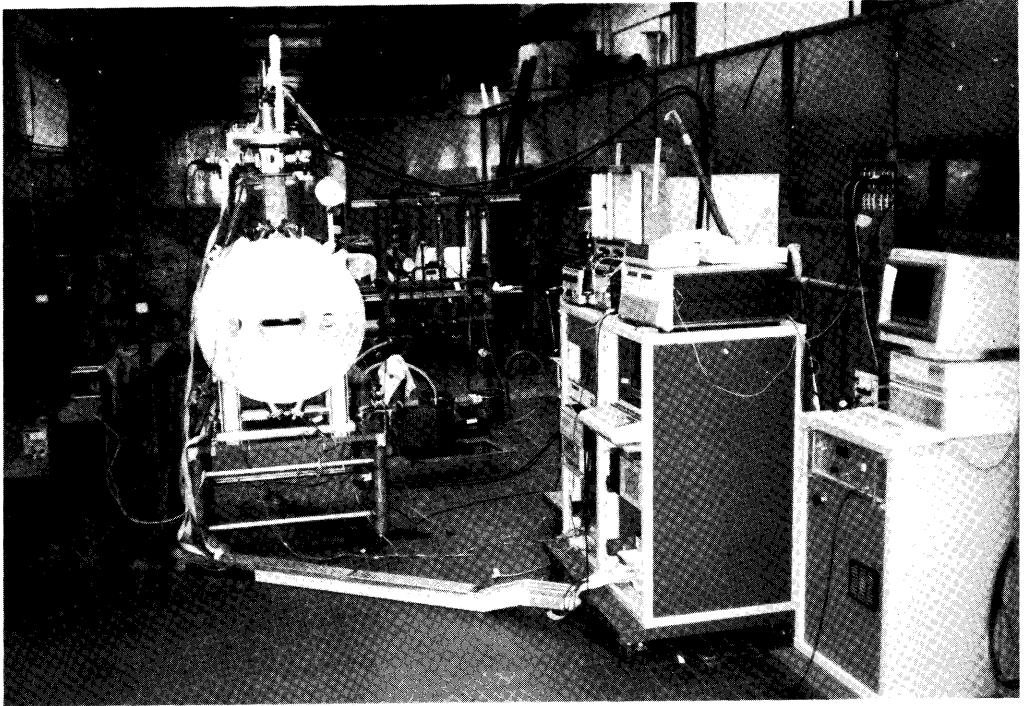
Fig. 42. – Wiggler under test: comprehensive view.

With this aim, we decided to use the helium vessel fiducial marks only to centre the magnet symmetry plane and centre line with respect to equivalent reference lines marked, through a precision milling machine, outside the cryostat flanges. These external marks represent the whole system symmetry axes, which are always accessible for the alignment operations. In other words: the helium vessel fiducial marks, presenting the magnet axes, are made to coincide with the external vessel symmetry axes by adjusting the eight supporting rods to which the helium vessel is suspended.

To achieve this operation, two view ports on both end plates of the vacuum container (see fig. 40) and also similar little holes in the radiation shield (see fig. 41), corresponding to the internal vessel fiducial marks, have been foreseen. After magnet cooldown, the fine levelling and centring operation are performed and the four view ports are blanked by flanges.

With the procedure described above, the levelling and centring operations proved to be very easy and no problems are expected when aligning the cryostat on the Adone orbit by means of the usual optical instruments.

It is clear that, during the wiggler operation, the Adone beam will be the most sensitive position monitor for the whole system (superconducting dipole plus compensator magnets); in any case it will be always possible, by opening the view ports and applying some simple optical devices, to make use of TV cameras to monitor the helium vessel alignment on line. For this reason the view ports optical glasses are equipped with gratings on which the internal fiducial marks should remain always

aligned, unless something goes wrong with the helium vessel or the suspension rods, during magnet operation. The experience gained with machine runs will tell us if the on-line position control described above will be necessary.

10. – Conclusion.

The field profile obtained, exceeding 6 T with high stability, is proof of the superconducting magnet reliability and confirms the design goal.

Magnetic measurements of the overall system to fulfill the storage ring specifications are the most important task for immediate future.

With this aim two kinds of magnetic measurements will be carried out as described in sect. 8:

point-to-point magnetic-field map in the horizontal plane where the beam lies;

field integral measurements along the magnet axis.

The field map measurements and the performances of the related equipment will be described in a paper to follow.

REFERENCES

[1] A. U. Luccio: *Status report on the Adone wiggler and X-ray beam line*, in *Wiggler Meeting, Frascati, June 29-30, 1978*.
[2] H. Hsieh et al.: *IEEE Trans. Nucl. Sci.*, Vol. NS-28, No. 3 (June 1981).
[3] S. Pissanetzky: *The new version of the finite element 3 D magnetostatics program Magnus*, in *Computational Electromagnetics*, edited by Z. J. Cendes (Elsevier Science Publishers B. V., North Holland, IMACS, 1986).
[4] R. Coisson, S. Guiducci and M. Preger: *Nucl. Instrum. Methods*, **201**, p. 3 (1982).
[5] M. Helm, M. J. Lee and P. L. Morton: *Evaluation of synchrotron radiation integrals*, SLAC/PUB - 1193 (March 1973).
[6] R. P. Walker: *An improved wiggler model: calculation of beam parameters and comparison with experiment*, SRS/APN/82/41.
[7] M. N. Wilson: *Superconducting Magnet* (Clarendon Press, Oxford, 1983), p. 200.
[8] C. Sanelli: *Progetto magnetico dei compensatori per S.CO.W.*, LNF-85/64 (R) (1985).